2.3 Electrical properties of the earth's interior

2.3.1 Depth distribution of the electrical conductivity

2.3.1.0 List of symbols and abbreviations

Table 1.

Symbols

$\overline{AB}$	electrode spacing in DC geoelectric soundings
C	C-response, see subsect. 4.2.2.2.3 for definition, in [km]
d_m	thickness of uniform layer
d_0	adjustable layer parameter, in [km]
D	thickness of high resistivity layer
h	thickness of non-conducting layer
I	direct current
l	half the distance between voltage electrodes, in [km]
L	half the distance between current electrodes, in [km]
m	logarithmic derivative of ϱ_a, eq. (5)
p	skin depth, eq (2) in 4.2.2
Q	Q-response, see subsect. 4.2.2.2.2 for definition
t	time
T	oscillation period, in [s] or [h]=hours, [d]=days, [a]=years
ΔU	voltage drop
$y(\omega)$	logarithmic response, eq. (8)
z	depth, in [km]
z^*	depth of substitute perfect conductor, eq. (6), in [km]
Z	Z-response (impedance), see subsect. 4.2.2.2.4 for definition, in [km/s]
ε^2	mean squared residual, eq. (11)
η	induction parameter
μ_0	magnetic permeability of vacuum, $\mu_0 = 4\pi \cdot 10^{-7}$ Vs/Am
ϱ	electrical resistivity, in [Ωm]
ϱ_a	apparent resistivity of substitute uniform half-space, eq. (2), in [Ωm]
ϱ_b	Niblett-Bostick apparent resistivity
ϱ^*	modified apparent resistivity of substitute uniform conductor, eq. (7), in [Ωm]
σ	root mean square error of logarithmic response $y(\omega)$
τ	thin sheet conductance, in [S] ($S=\Omega^{-1}$)
ϕ	phase of impedance, in degree
Φ	phase, $\Phi = \phi - \pi/4$
ω	angular frequency, $\omega = 2\pi/T$

Abbreviations

DP	disturbed polar geomagnetic variations
Dst	smoothed storm-time geomagnetic variations
S	solar daily geomagnetic variations

2.3.1.1 Introduction

Two classes of geophysical surface observations lead to estimates of the in-situ electrical conductivity of matter below the surface: direct current methods, used mainly to investigate sediments above the crystalline basement, and electromagnetic methods, penetrating through the basement downward into crust and mantle.

Since both methods are governed by Laplace type or diffusion type equations depth resolution is poor with regard to resistivity when compared to the resolution which is obtainable with propagating seismic waves in respect to seismic velocities. Hence, only mean values of resistivity over a certain depth range can be expected from experimental electric or electromagnetic data, even though the inverse problem to find $\varrho(z)$ as function

of depth z from ideal error-free data has a unique solution [Bai70, Wei72]. The restriction to layered earth models in which ϱ is a sole function of z adds to the ambiguity of interpretation.

Emphasis will be given therefore to data presentations in the form of depth profiles of apparent resistivity, which reveal already the essentials of the internal resistivity structure. Model interpretations are added to demonstrate the possible range of true internal resistivities, but note the comments on and the three basic deficiencies of any inversion of experimental data in subsect. 2.3.1.3.

2.3.1.2 Derivation of apparent resistivity estimates from experimental electric and electromagnetic data

Electric data: a direct current of known strength I is led into the ground with two electrodes at two points A and B, $L=\overline{AB}/2$, i.e. half the distance between points A and B. The voltage drop ΔU is measured with a second pair of electrodes at M and N, $l=\overline{MN}/2$. Let the four electrodes lie on a straight line with the current electrodes outside and the voltage electrodes symmetric to the center of $\overline{AB}$. Then

$$\varrho_a(L)=\frac{\pi\,\Delta U}{I}\left(\frac{1}{L-l}-\frac{1}{L+l}\right)^{-1} \tag{1}$$

defines the apparent resistivity $\varrho_a(L)$ of a substitute uniform half-space as function of current-electrode distance, with l either constant or a fixed fraction of L.

For a uniform earth $\varrho_a(L)$ is independent of L and equal to the true resistivity. For a non-uniform earth $\varrho_a(L)$ as function of L contains the information about $\varrho(z)$, since the penetration depth of electrical currents increases with L.

Electromagnetic data: a time-varying current source at or above the earth's surface produces the primary part of an electromagnetic surface field. Its secondary part comes from currents within the earth which are electromagnetically induced in conducting matter. The superposition of both parts is observed, in the case of natural sources, in the form of geomagnetic and geoelectric (=telluric) variations. See subsect. 4.1.1 about natural sources, and subsect. 4.2.2.1 for details of the induction process.

Electromagnetic surface observations are translated into response estimates as discussed in subsect. 4.2.2.2, usually in the frequency domain with $\exp(i\omega t)$ as time factor (ω: angular frequency). Three kinds of responses are considered: the Q-response, a dimensionless complex ratio of internal to external source contributions to the magnetic surface field; the C-response, a complex-valued penetration depth, in [km]; the Z-response, a complex scalar impedance, in [(mV/km)/nT]=[km/s]. Eqs. (8) and (16) in subsect. 4.2.2.2 connect Q, C, and Z with each other for a layered earth and a tangential electric source field. Note that for a given frequency $|C|$ defines an inductive scale length for the depth-distance range which determines the C- and Z-response and to which the restriction of a laterally uniform earth model applies.

The induction has an upper limit, set by self-induction, for which Q, but not C or Z, assumes an asymptotic value independent of $\varrho(z)$. The asymptotic values of C and Z define source-independent zero-wavenumber responses C_0 and Z_0, respectively. They are sole functions of $\varrho(z)$. See eq. (12) in subsect. 4.2.2.2 for conditions which allow the interpretation of empirical response estimates in terms of their asymptotic values.

The moduli of C_0 and $Z_0=i\omega C_0$ define, as function of frequency, the Cagniard-Tikhonov apparent electrical resistivity of a substitute uniform half-space:

$$\varrho_a(\omega)=\omega\mu_0|C_0(\omega)|^2=\frac{\mu_0}{\omega}|Z_0(\omega)|^2. \tag{2}$$

Insertion of $\mu_0=4\pi\cdot10^{-7}$ Vs/Am yields with C_0 in [km], Z_0 in [km/s], and oscillation period $T=2\pi/\omega$ in [s]

$$\varrho_a(\omega)=0.8\,\pi^2\omega|C_0|^2=0.2\,T|Z_0|^2\,[\Omega\mathrm{m}].$$

For a uniform earth $\varrho_a(\omega)$ is independent of frequency and equal to the true resistivity as seen from eq. (17b) in subsect. 4.2.2.2. For a non-uniform earth $\varrho_a(\omega)$ as function of frequency contains the information on $\varrho(z)$, since the penetration depth increases with decreasing frequency. But note that the phases of C_0 and Z_0, satisfying the relation

$$\phi(\omega)\equiv\arg\{Z_0(\omega)\}=\frac{\pi}{2}+\arg\{C_0(\omega)\}, \tag{3}$$

contain, as functions of frequency, the same information as ϱ_a except for a scaling resistivity ϱ_0.

This is a consequence of the dispersion relation, which connects, as functions of ω, real and imaginary parts of the response and thereby amplitude and phase. For C_0 it reads

$$C_0(\omega)=\frac{i}{\pi}\int_{-\infty}^{+\infty}\frac{C_0(\omega')\,d\omega'}{\omega-\omega'},$$

with Cauchy's principal value to be taken for the integral. The approximate version for amplitude and phase is

$$\Phi(\omega) \equiv \phi(\omega) - \frac{\pi}{4} \approx -\frac{\pi}{4} m \tag{4}$$

[eq. 2.28 in Wei72] where

$$m = \frac{T}{\varrho_a} \frac{d\varrho_a}{dT}. \tag{5}$$

Even though amplitude and phase appear to be redundant at least for ideal error-free data, they provide quasi-independent information for a *single* frequency:

$$z^*(\omega) = \mathrm{Re}\{C_0(\omega)\} = \mathrm{Im}\{Z_0(\omega)\}/\omega \tag{6}$$

defines the depth of a substitute perfect conductor, which is also the central depth of the in-phase induced currents (eq. (21) in subsect. 4.2.2). The imaginary part of C_0 (or Z_0^{-1}) adds information about the finite resistivity at this depth:

If $\phi > \pi/4$, $-2\,\mathrm{Im}\{C_0\}$ can be interpreted as skin depth of a uniform half-space of resistivity

$$\varrho^* = 2\omega\mu_0(\mathrm{Im}\{C_0\})^2 = 2\varrho_a \cos^2\phi = \varrho_a(1 - \sin 2\Phi), \tag{7a}$$

covered by a non-conducting layer of thickness

$$h = \mathrm{Re}\{C_0\} + \mathrm{Im}\{C_0\}$$

as seen from eq. (11) in subsect. 4.2.2.2. If $\phi < \pi/4$, then, according to eq. (19) in subsect. 4.2.2.2, $-\mathrm{Im}\{Z_0^{-1}\}\omega$ can be interpreted as reciprocal skin depth of a uniform half-space of resistivity

$$\varrho^* = \frac{\mu_0}{2\omega}(\mathrm{Im}\{Z_0^{-1}\})^{-2} = \frac{\varrho_a}{2\sin^2\phi} = \frac{\varrho_a}{1 + \sin 2\Phi}, \tag{7b}$$

covered by a thin conducting layer of conductance

$$\tau = \frac{1}{\mu_0}(\mathrm{Re}\{Z_0^{-1}\} + \mathrm{Im}\{Z_0^{-1}\}).$$

These relations define a modified apparent resistivity ϱ^* of a substitute uniform conductor when the effect of better or less conducting surface layers is removed, and provide with z^* for the same frequency a depth profile $\varrho^*(z^*)$ of apparent resistivities if the response is known for more than one frequency.

The effect of surface layers can be taken into account also by considering the change of ϱ_a with period as expressed by m in eq. (5). The Niblett-Bostick apparent resistivity is defined by

$$\varrho_b = \varrho_a \frac{1+m}{1-m}$$

[Jon83], which in combination with $|C|$ for the same frequency yields an alternative depth profile $\varrho_b(|C|)$ of apparent resistivities. Note that with the approximation of eq. (4)

$$\varrho_b \approx \varrho_a \frac{1 - \frac{4}{\pi}\Phi}{1 + \frac{4}{\pi}\Phi}$$

which eliminates the need to derive m from empirical response estimates. For small deviations of the phase from 45°, ϱ^* and ϱ_b are approximately equal to ϱ_a, the differences being proportional to Φ.

2.3.1.3 Inversion of electromagnetic response estimates

Inversion implies that a given set of response estimates for N different frequencies is explained by a resistivity model $\varrho(z)$. This can be an analytical expression for the depth dependence of ϱ or a layered model consisting of M uniform layers of resistivity ϱ_m and thickness d_m, $m = 1, 2, \ldots, M$ and $d_M = \infty$. See subsect. 2.3.1.5 for a transformation to spherical models. If M is not chosen sufficiently small in comparison to N (or infinite), mean values $\bar{\varrho}(z_k)$ for a certain target depth z_k are derived, providing a smoothed quasi-continuous approximation to the true earth model. Otherwise the approximation is by a discontinuous model with layer boundaries as pure artifacts for the chosen number of layers.

The following guidelines restrict the number of acceptable models: The maximum and minimum depth values z^* which result from $\mathrm{Re}\{C_0\}$ for the lowest and highest frequencies, respectively, limit the depth range for which the given data can resolve $\varrho(z)$, while ϱ^* (or ϱ_b) indicates the resistivity structure within this range. Any model found by inversion should have only those structural details which are visible and significant in the apparent resistivity profile. See [Par82] to find for a given set of responses the ultimate depth of a perfect conductor limiting the downward extent of interpretation.

In order to secure that the data set can be interpreted by any model $\varrho(z)$ at all, certain conditions have to be satisfied (in addition to the dispersion relation):

(i) The phase ϕ must lie between zero and 90°;

ii) the depth z^* of a perfect substitute conductor must not decrease with increasing period, i.e., $\mathrm{d}\,\mathrm{Re}\{C_0\}/\mathrm{d}T \geqq 0$;

(iii) the change of amplitude $|C_0|$ or $|Z_0|$ with period, expressed by the dimensionless ratio m in eq. (5), must not exceed the limits set by $|m| \leqq 1$.

See [Wei72] for a complete list of such inequalities.

Two methods are used to adjust empirical estimates to these conditions:

(i) They are smoothed and, if necessary, corrected to meet the inequalities and the dispersion relation as prerequisite for their exact interpretation by models;

(ii) empirical estimates are interpreted only approximately, allowing for a misfit between model and observations in the size of data errors.

The models in Figs. 9 and 12 have been derived from unsmoothed response estimates, using the ψ-algorithm as described in [Lar75]. Input datum is the logarithmic response

$$y(\omega) = \ln\{\mathrm{i}\,\omega\mu_0\, C_0^2(\omega)/\varrho_0\} = \ln\{\varrho_a(\omega)/\varrho_0\} + 2\,\mathrm{i}\,\Phi(\omega), \tag{8}$$

where ϱ_0 is an arbitrary scaling resistivity, here set to $\varrho_0 = 1\ \Omega\mathrm{m}$. This response has a quasi-linear relation to the logarithmic resistivity model $x(z') = \ln\{\varrho(z')/\varrho_0\}$, where

$$z'(z) = \int_0^z \sqrt{\varrho_0/\varrho(t)}\,\mathrm{d}\,t \tag{9}$$

defines a reduced depth scale. It enlarges depth zones of low resistivity and contracts zones of high resistivity in correspondence to the changing skin effect in them.

In detail: Let y_n denote a set of logarithmic response estimates for frequency ω_n ($n = 1, 2, \ldots, N$), Δy_n their errors. Then a set of M model parameters $x_m = \ln\{\varrho_m/\varrho_0\}$ is found by solving a system of linear equations, by a least-squares analysis for $M \ll N$, and by a generalized inverse technique for ill-conditioned linear problems otherwise [Wig72]. In the latter case a mean model parameter for the k-th target layer

$$\bar{x}_k = \sum_m a_{km}\, x_m \tag{10}$$

will be presented together with the averaging kernel $A = (a_{km})$.

Model errors Δx_m and $\Delta \bar{x}_k$, respectively, are derived from the data errors, and the misfit between observed (y_n) and model responses (y_n^*) is expressed by the mean squared residual

$$\varepsilon^2 = \frac{1}{N} \sum_n |y_n - y_n^*|^2. \tag{11}$$

For values small compared to unity, ε is the relative discrepancy between observed and calculated apparent resistivity ϱ_a; alternatively, $\varepsilon/2$ is the discrepancy in phase ϕ (in angular measure) as seen from eq. (8).

In this approach to inversion the layer thickness is not treated as a free model parameter, but is, for a model resistivity ϱ_m, derived from

$$d_m = d_0 \sqrt{\varrho_m/\varrho_0}; \tag{12}$$

d_0 is an adjustable layer parameter. Eq. (12) implies that the model is equally subdivided into layers of constant thickness d_0 when transferred to the reduced depth scale z' of eq. (9). In the search for a bestfitting model of a chosen number of layers M, d_0 is that value which minimizes ε^2.

2.3.1.4 Principle constraints of interpretation

Theoretical response functions, represented in Figs. 1 ··· 3 in the form of $\varrho^*(z^*)$ diagrams, demonstrate the following constraints for any interpretation of empirical response estimates:

1. The response for a gradual transition between depth regions of different resistivity is very close to the response for a discontinuous change (Fig. 1).

2. For a well conducting intermediate layer only the depth-integrated total conductivity or conductance τ can be determined with accuracy (Fig. 2). The same applies to thin surface layers above a less conducting substratum, in particular when response estimates are restricted to low frequencies for which the penetration depth exceeds the thickness of the top layer.

3. For a high resistivity layer which is shielded by conducting surface layers at the top and underlain by a very good conductor only a lower bound for its resistivity ϱ_R is obtainable if ϱ_R exceeds a certain threshold value ϱ_T (Fig. 3).

In detail: Let τ be the conductance of the surface layers and D be the thickness of the high resistivity layer. Then the dimensionless induction parameter $\eta=\omega\mu_0\tau D$ has to be below unity to allow for substantial induction within this layer. On the other hand, it acts like an insulator of infinite resistivity unless its skin depth $p=\sqrt{2\varrho_R/\omega\mu_0}$ at the frequency for which η reaches unity is less or about equal to D. Hence, to be distinguishable from an insulator, ϱ_R should be below the threshold $\varrho_T=D/2\tau$ applying to the limiting case that $p\approx D$ and $\eta\approx 1$.

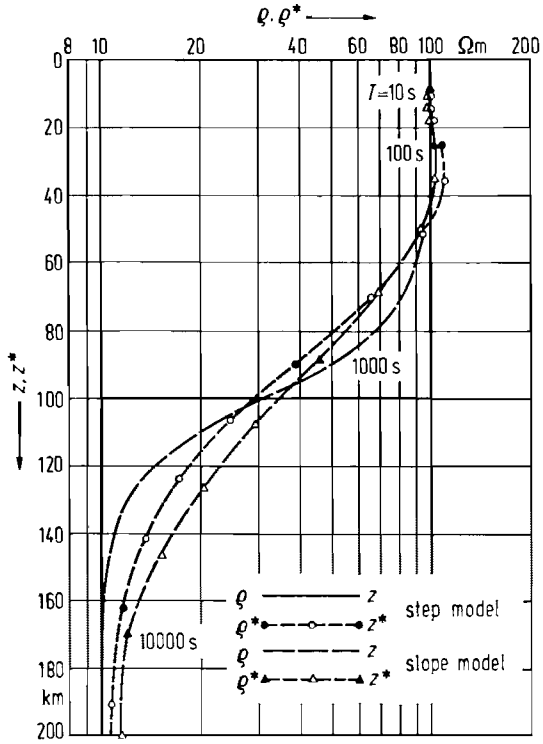

Fig. 1. Theoretical response curves, periods from 10000···10 s, are compared for two models: a 2-layer model and a continuous model with a discontinuous and a gradual change in resistivity, respectively. Their responses, displayed as apparent resistivity $\varrho^*(z^*)$ diagrams, are close to each other, which can make the models undistinguishable for empirical response estimates with errors. – Four responses per decade on an equally subdivided logarithmic frequency scale.

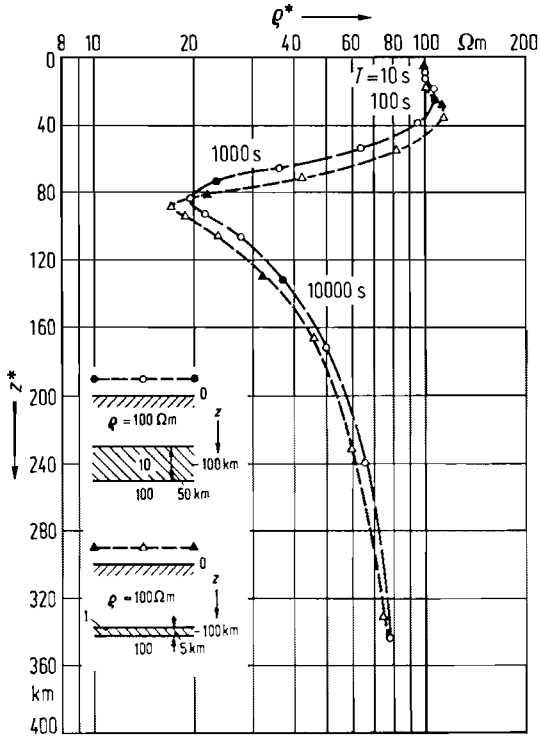

Fig. 2. Theoretical response curves, periods from 56000··· 10 s, are compared for two models with a well conducting intermediate layer. Its thickness and resistivity differ by factors of ten, but the product thickness times conductivity is constant. The closeness of the model responses, shown in the form of apparent resistivity $\varrho^*(z^*)$ diagrams, demonstrates that with empirical responses only the conductance may be a resolvable parameter for the intermediate layer. – Four responses per decade on an equally subdivided logarithmic frequency scale.

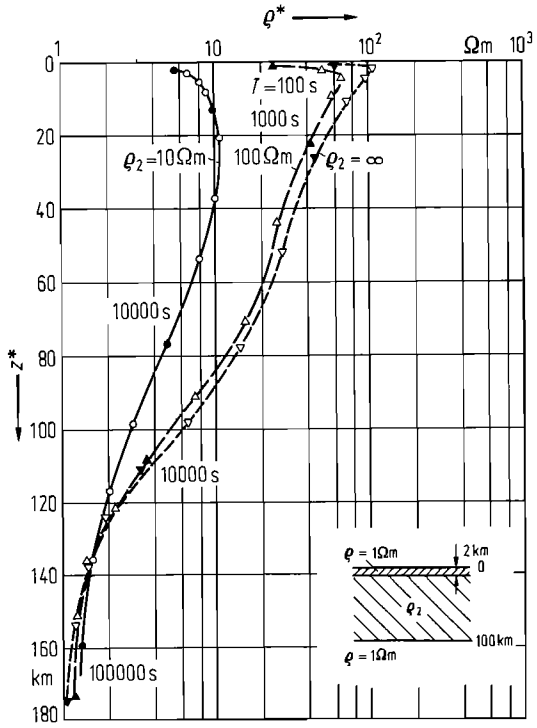

Fig. 3. Theoretical response curves, periods from 100000··· 100 s, are compared for 3-layer models: a thin conducting top layer (conductance: 2000 S), a high-resistivity intermediate layer of variable resistivity ϱ_2, a well conducting uniform substratum. The threshold value ϱ_T for ϱ_2, quoted in the text, is 25 Ωm. A comparison of the $\varrho^*(z^*)$ diagrams demonstrates that the intermediate layer may not be distinguishable from a perfect non-conductor unless $\varrho_2 < \varrho_T$ when empirical responses with errors are interpreted. – Four responses per decade on an equally subdivided logarithmic frequency scale.

2.3.1.5 General notes on response data and models in figures and tables of subsection 2.3.1

The data source for the following subsects. 2.3.1.6···2.3.1.8 can be found in original form in Tables 2···12 of sect. 4.2.2. Depending on the method of determination, one of the following response estimates is tabulated: $Q_n(\omega)$, $C_n(\omega)$ or $C_0(\omega)$, $Z_n(\omega)$. See the legends to these tables for the sources and symbols which are used also in this section to identify the various sets of response estimates.

For S, Dst, and very long period variations, a complete collection of available response estimates has been attempted: Tables 2···7 and Table 9 of subsect. 4.2.2. Here only the most self-consistent data sets are retained.

For polar substorm variations and pulsations, eight representations of response estimates have been selected from a large number of published magnetotelluric results, four for continents and four for oceans: Tables 11 and 12 of subsect. 4.2.2. Also included in the following are the response estimates from Table 8 of subsect. 4.2.2, obtained with the magnetic gradient method, and two magnetotelluric results (EEP, RAB) which are not quoted in subsect. 4.2.2. Details on them can be found in subsect. 2.3.1.6.

Each data set is presented in

(i) figures with apparent resistivity $\varrho^*(z^*)$ diagrams,

(ii) figures with models derived from the response,

(iii) tables with apparent resistivities, phases, and depth values z^*.

Fig. 11 presents for selected data apparent resistivities ϱ_a and phases ϕ as a function of period T. The tabulated response values are grouped into period bands to allow a joint presentation of different data sets for the same period range. See the cited tables of subsect. 4.2.2 to find the exact period to which the tabulated values refer.

The models are reproduced from the cited sources. When errors of the model parameters are given, they are from a new interpretation using the ψ-algorithm as described in subsect. 2.3.1.3.

For a selection of models, theoretical responses have been calculated. They are tabulated in Tables 10···13 for S, Dst, and very long period variations, in Table 14 for substorm variations. The models do not include crustal conductors or conducting surface layers or oceans. If they are to be added, find the new response C' from

$$C'(\omega) = C_0(\omega)/[1 + i\,\omega\,\mu_0\,\tau\,C_0(\omega)]; \tag{13}$$

τ is the conductance of the crustal or surface conductors, which are regarded as thin sheets, and $C_0(\omega)$ the tabulated response for a plane earth. For a spherical earth model, apply the conversion to the Q-response:

with

$$Q'_n(\omega) = \left[Q_n(\omega) + \frac{n}{n+1}\,i\,\eta_s\right] \Big/ (1 + i\,\eta_s) \tag{14}$$

$$\eta_s = \omega\,\mu_0\,\tau\,R_E \left[1 - \frac{n+1}{n}\,Q_n(\omega)\right] \Big/ (2n+1).$$

2.3.1.6 The electrical resistivity in the continental crust

Magmatic and metamorphic rocks can be expected to be poor conductors under crustal conditions with resistivities well above 10000 Ωm. See the subsections 5.1.2.1 and 5.1.2.2 in [Ang82], and [Kar83] for a collection of relevant laboratory and in-situ determinations. Where the crystalline basement is covered by better conducting sediments, electromagnetic methods cannot resolve its extremely high resistivity as demonstrated in Fig. 3. The threshold value quoted in subsect. 2.3.1.4 will be exceeded even under moderate sedimentary cover.

Information about the resistivity in the upper crust comes therefore mainly from direct current methods with large electrode spacings, which, in contrast to electromagnetic methods, resolve poor conductors below screening sediments because the current must pass through them.

Figure 4 shows examples from South Africa. It is found that in this specific shield area unfractured blocks of granite and gneiss have a resistivity between 30000 and 400000 Ωm down to a depth of 5···10 km [Vzi78]. Fold Belts with fractured and highly metamorphic rocks are in comparison better conducting with 2000··· 10000 Ωm. Similar studies in central Europe verified the great variability in the resistivity of basement rocks, ranging here from less than 1000···18000 Ωm [Blo80]. Average values are quoted as 100000 Ωm for the unfractured crystalline basement and as 5000 Ωm for Fold Belts [Vzi78]. For the change of basement resistivities with pressure and temperature according to laboratory data, see [Kar83].

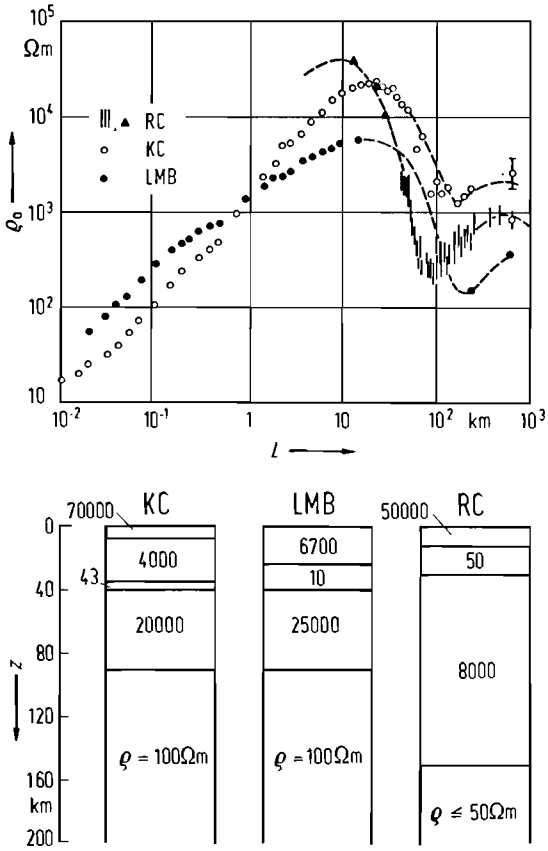

Fig. 4. Direct-current sounding experiments with very long electrode distances $\overline{AB} = 2L$ on the Precambrian shield of Southern Africa. RC: Rhodesian craton [Blo77]; KC: Kapvaal craton [Vzi78]; LMB: Limpopo Mobile Belt [Vzi78]. The maximum electrode spacing is about 1500 km which puts currents through the entire crust. – The displayed apparent resistivities ϱ_a as functions of electrode spacing show distinct peak values of 5000···20000 Ωm for 20··· 40 km electrode spacing, indicating an upper crust of high, but variable resistivity. The steep descent to a ϱ_a minimum between 200 and 1200 Ωm close to L=100 km is unambiguous evidence for a deep crustal conductor. See Fig. 8 for magnetotelluric evidence for such conductors. The following ascent of ϱ_a toward greater electrode distances proves the existence of again high resistivities in the uppermost mantle. The onset of a secondary descent, visible only for RC, suggests a lower bound for the uppermantle resistor at, say, 150 km depth. – The layered models below are from the quoted sources. Thin conducting top layers to explain the ascending ϱ_a values for small electrode distances are ignored.

Figure 5 represents the results of magnetotelluric studies in the period range relevant for investigations of the crust. The data selection has been such that it covers the range of conductance for continental surface layers with a minimum of distortion by local heterogeneities in them.

The response values ϱ_a, ϱ^*, ϕ^*, and z^* for the soundings of Fig. 5 can be found in Tables 2···9 with information on the data source.

For a shallow penetration depth within the sedimentary cover, if any, ϱ^* varies in correspondence to the true resistivity of the sediments. See subsections 5.1.2.3 and 5.1.2.4 in [Ang82] for laboratory and in-situ resistivities of consolidated and unconsolidated sediments. But note that the effective resistivity of sediments from magnetotelluric and direct current investigations is considerably below the tabulated values. Consult section 5.3 in [Ang82] for the decisive influence of porosity and conductivity of the pore fluids. A world map for the conductance of sediments and oceans has been compiled by Fainberg and Sidorov [Fai78].

As seen from Fig. 7, the sediments of the North German basin (TEW) and the Rhine Graben (SIG) have resistivities of 1 Ωm, which appears to be typical of unconsolidated sediments of high porosity and high salt content of the pore fluids. Consolidated sediments are more resistive (10···100 Ωm), but the presented soundings SCA, NEW do not include sufficiently high frequencies to resolve the uppermost sedimentary cover. For PLE a conductance of 10 S is quoted, while ϱ^* approaches the quoted values of the crystalline basement.

The apparent resistivity ϱ^* at crustal depth ($z^* = 20$ km) varies from 20 Ωm for the North German Basin (TEW) and the Rhine Graben (SIG) to more than 10000 Ωm in an exposed crystalline complex (PLE). Because in the derivation of ϱ^*, in contrast to ϱ_a, the shielding effect of surface layers is removed, the observed variability of upper crustal resistivity should be real. This is exemplified by the models in Fig. 6.

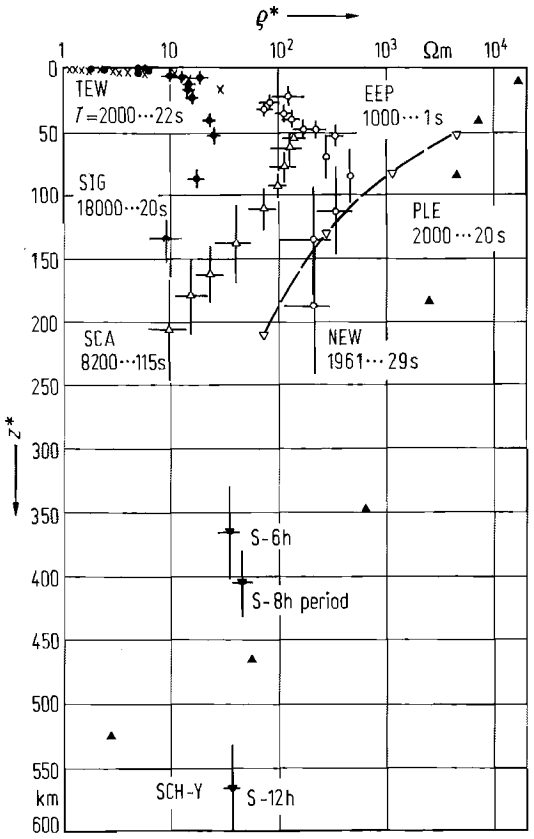

Fig. 5. Apparent resistivity $\varrho^*(z^*)$ diagrams for pulsations and polar substorm variations at selected continental sites: PLE: Belorussian massif with exposed crystalline basement rocks; NEW: paleozoic fold belt in Southern Scotland; SIG: Rhine Graben rift zone in Southwestern Germany; TEW: Deep sedimentary basin in Northern Germany. The response estimates are from magnetotelluric soundings in the indicated period ranges. See Table 11 in 4.2.2 for the periods of individual response estimates and the data sources. The curve labeled EEP refers to the combined descending branches of eleven selected $\varrho_a(T)$-curves on the East European platform [Vla72]. The estimates labeled SCA refer to geomagnetic gradient soundings in Scandinavia (cf. Table 8 in 4.2.2). For comparison response estimates for three subharmonics of diurnal S variations from Fig. 10 are added. See Fig. 7 and 8 for presentations of NEW, SIG and TEW on expanded depth scales.
For short periods and shallow depths of penetration, the wide span in apparent resistivities from 1···20000 Ωm reflects the variability of continental surficial resistivities between water-saturated, unconsolidated sediments and dry igneous rocks. At subcrustal depth the sounding curves are drawn together to a range from 20···5000 Ωm. See in Fig. 6 for a presentation by models. Beyond 50 km depth of penetration all ϱ^*-values decrease with increasing period, reflecting a gradual or discontinuous resistivity decrease within the upper mantle. See again Fig. 6 and the text for details. No response estimates exist between 200 and 360 km depth. See Figs. 10 and 12 for results from long period variations, and Fig. 15 for results from oceans.

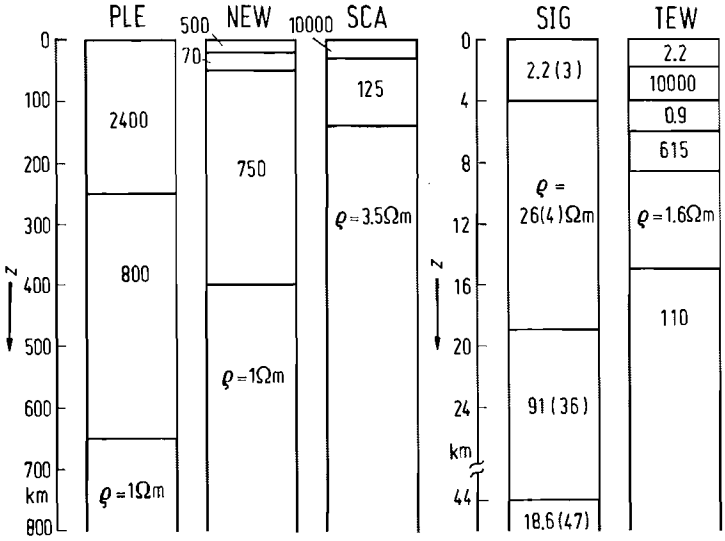

Fig. 6. Layered resistivity models from quoted sources in Table 11, subsect. 4.2.2, to interpret the response data shown in Fig. 5. The numbers give the layer resistivities in units of 1 Ωm. The input response values are listed in Tables 2···5.

Table 2. Apparent resistivity ϱ_a derived from the response of polar storms, substorms, and pulsations at continental sites. The evaluated response estimates are listed and explained in the tables of subsect. 4.2.2: SCA = Scandinavia: Table 8; TUC = Tuscon: Table 10; PLE, NEW, SIG, TEW: Table 11. * implies a combined estimate from two listed values at adjacent frequencies.

T h	ϱ_a Ωm			
	TUC	SCA		SIG
5.0···5.3	127			12.6(26)
2.8···3.2	122			
2.3···2.5		46(17)		15.5(13)
1.66				14.3(8)
1.0···1.25		70(22)		12.1(6)*

T s	ϱ_a Ωm				
	PLE	SCA	NEW	SIG	TEW
1800···2500	1120	95(25)	245(105)	8.9(6)	8.9(18)
1200···1500		120(50)	205(115)	7.5(5)	
890···1100	1780	145(40)	255(95)	6.6(4)	5.0(6)
600···800			265(60)	5.5(8)	3.2(4)
400···590	2240	175(25)	210(30)*	5.0(9)	2.5(2)
300···390		205(55)	155(15)	3.4(5)*	2.0(2)
200···290	2670		160(25)		1.9(1)
150···190		235(75)	140(20)	2.0(3)	1.6(1)
100···140	2240	280(60)	145(10)	2.0(3)	1.50(5)
65···95			155(10)*	2.0(4)	1.2(1)
40···60	2000		175(20)*	1.9(1)	1.1(1)
25···35			205(70)	1.5(1)	1.0(1)
15···20	1500			1.4(1)	1.1(2)

Table 3. Modified apparent resistivity ϱ^* derived from the response of polar storms, substorms, and pulsations at continental sites. See legend to Table 2 for further explanations.

T h	ϱ^* Ωm				
Period	TUC	SCA		SIG	
5.0···5.3	69			9.3(19)	
2.8···3.2	80				
2.3···2.5		10(4)		18.0(15)	
1.66				26.1(14)	
1.0···1.25		16(5)		22.8(11)*	
T s	ϱ^* Ωm				
	PLE	SCA	NEW	SIG	TEW
1800···2500	3	23(6)	200(85)	15.6(10)	29.1(59)
1200···1500		42(17)	205(115)	15.0(10)	
890···1100	110	73(19)	335(125)	15.1(10)	15.1(18)
600···800			470(105)	19.1(27)	11.4(14)
400···590	630	99(15)	290(40)*	12.1(24)	5.9(4)
300···390		114(30)	215(20)	10.4(18)*	4.2(3)
200···290	2670		175(25)		3.6(2)
150···190		126(40)	130(15)	5.1(8)	3.0(2)
100···140	4480	141(31)	115(10)	6.5(9)	2.6(1)
65···95			79(5)*	6.2(13)	1.8(1)
40···60	7130		89(14)*	5.0(4)	1.6(1)
25···35			123(40)	2.4(1)	1.2(1)
15···20	17000			1.8(2)	1.1(2)

Table 4. Phase ϕ of the impedance of polar storms, substorms, and pulsations at continental sites. See legend to Table 2 for further explanations.

T h	ϕ degree			
	TUC	SCA	SIG	
5.0···5.3	58		53(6)	
2.8···3.2				
2.3···2.5	55	71(11)	41(2)	
1.66			32(2)	
1.0···1.25		70(9)	31(2)*	

continued

Table 4 (continued)

T s	ϕ degree				
	PLE	SCA	NEW	SIG	TEW
1800···2500	88	70(7)	50(12)	32(2)	23(6)
1200···1500		65(11)	45(16)	30(2)	
890···1100	80	60(8)	38(11)	28(2)	24(3)
600···800			32(7)	22(4)	22(4)
400···590	68	58(5)	38(5)*	26(5)	29(2)
300···390		58(8)	37(3)	24(5)*	29(3)
200···290	45		43(4)		31(1)
150···190		59(9)	47(4)	26(4)	31(2)
100···140	30	60(6)	51(2)	23(4)	33(1)
65···95			60(2)*	24(6)	35(2)
40···60	22		60(3)*	26(2)	35(2)
25···35			57(9)	34(1)	40(3)
15···20	12			38(3)	45(5)

Table 5. Depth z^* of perfect substitute conductor derived from the response of polar storms, substorms, and pulsations at continental sites. See legend to Table 2 for further explanations.

T h	z^* km		
	TUC	SCA	SIG
5.0···5.3	475		135(17)
2.8···3.2	345		
2.3···2.5		206(38)	87(6)
1.66			54(3)
1.0···1.25		180(26)	41(2)*

T s	z^* km				
	PLE	SCA	NEW	SIG	TEW
1800···2500	530	163(33)	190(55)	24.1(14)	18.6(48)
1200···1500		138(20)	135(55)	16.8(11)	
890···1100	470	111(16)	115(35)	12.7(9)	10.2(15)
600···800			85(20)	7.7(14)	6.3(11)
400···590	350	92(6)	70(15)*	7.4(16)	5.7(5)
300···390		78(15)	50(5)	4.8(11)*	4.2(3)
200···290	180		50(5)		3.5(1)
150···190		64(16)	41(4)	2.7(5)	2.8(2)
100···140	84	55(9)	38(2)	2.0(4)	2.3(0)
65···95			34(1)*	1.7(5)	1.8(1)
40···60	42		27(2)*	1.6(1)	1.5(1)
25···35			23(4)	1.3(1)	1.3(1)
15···20	13			1.2(1)	1.2(2)

Table 6. Apparent resistivity ϱ_a derived from the response of solar daily S variations, Dst ring current variations, and very long period variations. The evaluated response estimates are listed and explained in the tables of subsect. 4.2.2: S: Tables 3 and 7; Dst: Tables 2 and 6; very long period: Table 9.

Variation	T	ϱ_a Ωm				
		CHA	BER	MAL	FAI	SCH-Y
S	6 h	81	71(15)	63(34)	90	66(15)
	8 h	71	50(21)	59(20)	68	69(10)
	12 h	45	41(6)	53(17)	52	77(6)
	24 h	58	44(4)	43(22)	59	54(5)
		ECK	BAN	DEV	FAI	SCH
Dst	1.3···1.6 d			45(13)		28(3)
	2.7···3.0 d			22(4)	19	22(2)
	4.0···5.3 d			13(1)	20	
	8···10 d	5.2(48)	6.5(6)[1]			8.6(8)
	11···13 d		4.7(5)			6.2(10)
	20···25 d	4.6(46)	3.5(10)	3.9(6)	4.0	4.1(10)
		RIK	BAN	ISI	HAR	DUC
Very	27 d	7.4(16)	3.7(4)			
long	1 a		0.9(3)			
period	11 a			0.2(0.7)	0.11(6)	0.11(3)

[1]) 27 d periodicity with subharmonics.

Table 7. Modified apparent resistivity ϱ^* derived from the response of S, Dst, and very long period variations. See legend to Table 6 for further explanations.

Variation	T	ϱ^* Ωm				
		CHA	BER	MAL	FAI	SCH-Y
S	6 h	35	52(11)	45(25)	3	34(8)
	8 h	26	10.7(44)	29(10)	26	48(7)
	12 h	22	0.5(1)	19(6)	1	37(3)
	24 h	12	1.3(1)	(0)	13	4.4(4)
		ECK	BAN	DEV	FAI	SCH
Dst	1.3···1.6 d			15(5)	3.7	2.6(3)
	2.7···3.0 d			7(1)	2.6	1.8(2)
	4.0···5.3 d			1.8(2)		
	8···10 d		0.30(3)			0.30(3)
	11···13 d		1.6(2)	0.40(3)		0.6(1)
	20···25 d	0.9(2)	0.8(3)	0.06(1)	0.8	0.6(2)
		RIK	BAN	ISI	HAR	DUC
Very	27 d	2.2(5)	0.7(0.7)			
long	1 a		0.05(2)			
period	11 a			0.21 (8)	0.001	0.04(1)

Table 8. Phase ϕ of the impedance of S, Dst, and very long period variations. See legend to Table 6 for further explanations.

Variation	T	ϕ degree				
		CHA	BER	MAL	FAI	SCH-Y
S	6 h	62	53(6)	53(16)	83	60(7)
	8 h	65	71(12)	60(10)	64	54(4)
	12 h	60	85(4)	65(9)	84	60(2)
	24 h	71	82(2)	90(15)	71	78(3)
		ECK	BAN	DEV	FAI	SCH
Dst	1.3···1.6 d			66(8)		78(3)
	2.7···3.0 d			67(5)	72	78(3)
	4.0···5.3 d			74(3)	75	
	8···10 d	82(27)	81(3)			82(3)
	11···13 d		66(3)	80(2)		77(5)
	20···25 d	72(29)	71(8)	85(4)	72	74(7)
		RIK	BAN	ISI	HAR	DUC
Very	27 d	67(6)	72(3)			
long	1 a		80(8)			
period	11 a			43(10)	87(16)	66(7)

Table 9. Depth z^* of the perfect substitute conductor derived from the response of S, Dst, and very long period variations. See legend to Table 6 for further explanations.

Variation	T	z^* km				
		CHA	BER	MAL	FAI	SCH-Y
S	6 h	420	350(50)	330(110)	(500)	365(50)
	8 h	(460)	400(90)	400(80)	450	405(35)
	12 h	430	470(40)	490(90)	530	565(25)
	24 h	750	690(30)	680(180)	760	750(35)
		ECK	BAN	DEV	FAI	SCH
Dst	1.3···1.6 d			730(120)		690(40)
	2.7···3.0 d			750(70)	760	780(40)
	4.0···5.3 d			830(50)	890	
	8···10 d	750(350)	790(40)			860(40)
	11···12 d		760(40)	920(40)		900(80)
	20···25 d	950(500)	830(130)	960(80)	990	1020(130)
		RIK	BAN	ISI	HAR	DUC
Very	27 d	1360(160)	1000(50)	1500(400)		
long	1 a		1860(280)			
period	11 a			2000(500)	2200(600)	2000(250)

Figure 7 repeats the sounding results in the North German basin and in the Rhine Graben on an expanded depth scale to demonstrate the details which such plots can reveal already by visual inspection: The sharp rise in apparent resistivity at 2···3 km in the Rhine Graben (SIG) and at 6 km depth in Northern Germany (TEW)

corresponds to the transition from young unconsolidated to older consolidated sediments. For Northern Germany an extremely well conducting intermediate layer is proposed between 8 and 12 km depth. Such good conductors within the crust are not exceptional.

Figure 8 presents two examples with similar crustal conductors. They are prominent in the $\varrho^*(z^*)$ plots and thus not possible artifacts of the interpretation by models. The sounding curve NEW for southern Scotland has a ϱ^* minimum of 80 Ωm at 35 km depth, which in the model of Fig. 6 is interpreted by a layer of 70 Ωm between 35 and 50 km with adjoining regions of tenfold increased resistivity.

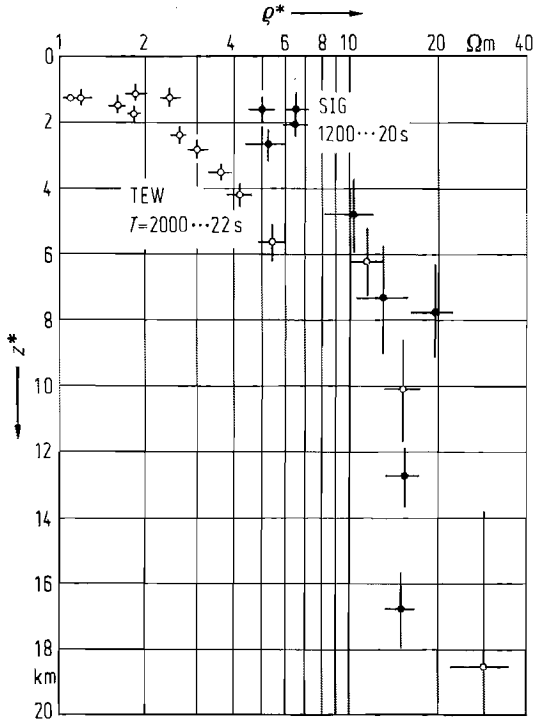

Fig. 7. Apparent resistivity $\varrho^*(z^*)$ diagrams for soundings TEW and SIG from Fig. 5 on an expanded depth scale to display structural details at shallow depth (cf. text). Note that $\varrho^* = 29$ Ωm at 1200 s for SIG is the maximum apparent resistivity, indicating an unusually low true resistivity of crust and uppermost mantle. See subsect. 2.3.2 for other evidence on low upper mantle resistivities beneath the Rhine Graben.

Fig. 8. Apparent resistivity $\varrho^*(z)$ diagrams for pulsations and polar substorm variations obtained at undistorted sites in paleozoic fold belts. RAB: Rhenish massif; NEW: Southern Scotland, see quoted source in Table 11 of 4.2.2. They give clear evidence for crustal or subcrustal conductors by minimum ϱ^* values at 12 km depth (RAB) and at 35 km depth (NEW). Model resistivities are 10 Ωm for RAB and 70 Ωm for NEW (cf. Fig. 6). Estimates of the conductance of the intermediate layers are 960 and 500 S, respectively. Numbers refer to the period of estimates in [s]. – Sounding curve RAB courtesy of K. Bahr. See also Joe [83].

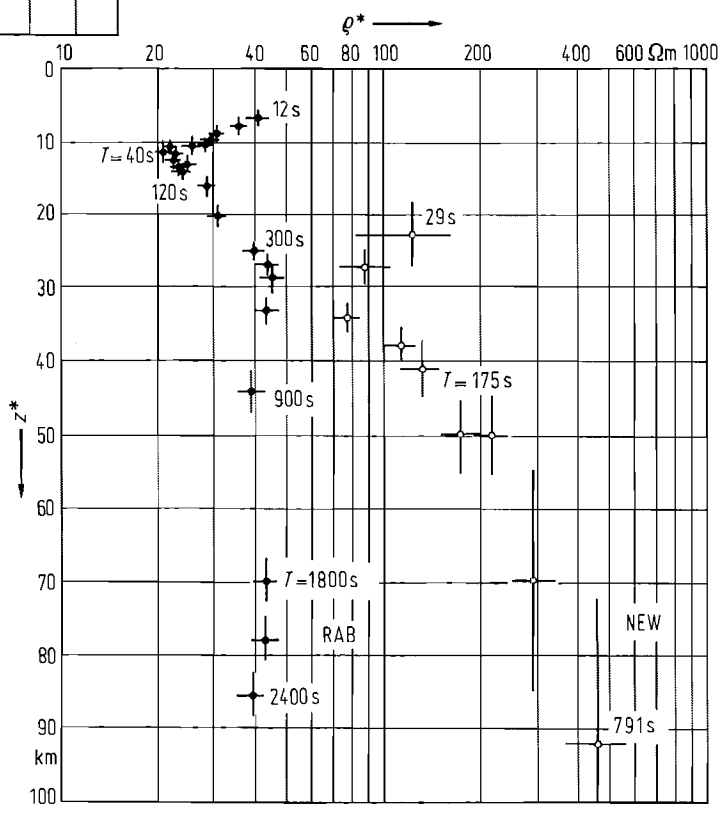

The sounding curve RAB for a station in the southern Rhenish massif in Germany indicates an even better conducting crustal zone with a ϱ^* minimum at only 12 km. It has been traced across the entire Rhenish massif in varying thickness and depth [Joe83]. The resistivity in this crustal conductor is estimated to lie between 5 and 50 Ωm, but it should be recalled from subsect. 2.3.1.4 that in such cases only the conductance of the intermediate layer is a resolvable quantity. In the case of RAB the conductance is 960 S.

The direct current sounding curves in Fig. 4 leave also no doubt about the presence of deep crustal conductors. At the bottom of this figure model resistivities between 10 and 50 Ωm are proposed for them in agreement with the above cited results for the Rhenish massif. On the other hand, the absence of crustal conductors is also clearly established for many regions. Fig. 5 gives two examples:

The response estimates SCA for Scandinavia have been obtained by applying the gradient method to an array of magnetometer stations below the polar electrojet. See subsect. 4.2.2.2.3 for a description of this method, which yields regionally smoothed response estimates. The gradual increase of ϱ^* with decreasing depth z^* suggests an equally gradual increase of true resistivity towards the surface with no indication of a crustal intermediate conductor. This has been verified with local magnetotelluric observations [Jon82]. See also the model interpretation for SCA in Fig. 6.

The magnetotelluric sounding curve EEP for the East European platform is to be understood as a regional average curve from 11 selected individual soundings with minimum distortion by surface layers [Vla72]. It gives no indication of either a crustal or asthenospheric conductor. Since it is also representative of many sounding curves in Karelia on the Baltic Shield [Kai83], the EEP curve has been suggested as a normal reference standard for investigations of crust and upper mantle to define local deviations as they arise, for instance, from intermediate conducting layers [Van77, Van80].

In the double logarithmic presentation of the period dependence of the apparent resistivity ϱ_a, the EEP curve is a straight line (Fig. 11). Its analytic expressions for amplitude and phase in the period range of validity, quoted as 1···10000 s, are

$$\log \varrho_a = 4.37 - 0.59 \log T, \tag{15}$$

$$\phi \approx 71.6°,$$

with ϱ_a in [Ωm] and T in [s]. The unspecified phase has been added, using eq. (4).

The unexpected presence of interspersed low resistivity zones within the crust has no obvious relation to geological or to other geophysical observations. It is found in comparable form under stable shields (South Africa) and regions of intense recent volcanism (Iceland; cf. subsect. 2.3.2.7), but is absent from other shields and geothermal areas (East European Platform, Scandinavia, Karelian Megabloc). See [Kar82] for an annotated bibliography on laboratory data relevant to low crustal resistivities. Current theories to explain deep crustal conductors propose the presence of free water in deeper sections of the crust, of hydrated minerals, such as serpentine, of sulphides, or of free carbon in the form of graphite [Dub82].

2.3.1.7 The electrical resistivity of the mantle from observations on continents

The upper mantle poses considerable problems for electromagnetic investigations: Magnetotelluric soundings reach only at exceptional places further down than, say, 200 km. The required periods for this penetration depth approach or exceed one hour and there is an increasing amount of telluric distortion. Purely magnetic methods, which would be less affected by shallow inhomogeneities, are either restricted to narrow regions of great source field inhomogenity, i.e. the auroral zone, or they require source fields with a well defined and reproducible structure. This applies to the sources of S and Dst variations, but the highest resolvable harmonic of S variations has already a period of six hours and a penetration depth well beyond 300 km. Thus a gap of direct information exists for the range from 200 to 350 km, as is clearly seen in Fig. 5.

Noting this basic deficiency of existing data, the following conclusions can be drawn from a joint interpretation of DP, S, and Dst variations: As seen from the models in Figs. 4 and 6, the uppermost mantle is a structureless poor conductor with resistivities of about 100 Ωm. Where good conductors in the lower crust are absent, a smooth transition from a more resistive crust is observed across the seismic Mohorovičič discontinuity. But note that an associated discontinuous change in resistivity would be undetectable with electromagnetic methods (Fig. 1). Where good crustal conductors exist, the subsequent increase of apparent resistivities is well established (Fig. 4 and 8). Regional difference may exist and, notably, rift zones are distinguished by low upper mantle resistivities. The results for the Rhine Graben station SIG are an example (Fig. 6).

In the adjoining depth range, which is still accessible to magnetotelluric soundings under favorable conditions, a definite tendency is observed for ϱ^* to decrease with increasing period and penetration depth. As a consequence, models to explain this decrease propose unbounded good conductors for the lower part of the

upper mantle, e.g. NEW and SCA in Fig. 6. They are in conflict, however, with response estimates for S variations with apparent resistivities ϱ^* of 20···50 Ωm for 6···12 h period (Table 7). In the response estimates SCH-Y a slight tendency is observed that even ϱ^* increases with increasing period and depth.

The response of S variations requires that the good conductor seen by magnetotelluric soundings is bounded and that the mantle resistivity must rise again to a second maximum. Fig. 9 presents models for a joint interpretation of S-Dst and those DP variations where the data already suggest the existence of an upper mantle conductor. It should be noted, however, that this brings together data sets of very different origin and that a large gap in periods exists. Fig. 10 shows the $\varrho^*(z^*)$ diagram of the responses used to derive these models.

They are instructive about the conductance and depth of the upper mantle conductor which is resolved in both models. Another important consequence arises for the adjoining deeper portion of the mantle. To be consistent with both DP and S-Dst response the resistivity below the mantle conductor must be extremely high again, i.e. greater than 100 Ωm, down to 700···800 km depth. This conclusion is supported by model interpretations of S-Dst responses alone, without DP in Fig. 10. Existing DP responses for regions where the upper mantle conductor is definitely absent, e.g. the East European platform, do not yet permit such a combined interpretation (see below).

The lower bound of the high resistivity mantle zone is again clearly established by the gradually decreasing ϱ^* values for increasing periods, starting with the fundamental period of S variations. Fig. 10 shows them in a $\varrho^*(z^*)$ diagram. The pertinent response values can be found in the Tables 6···9. The basic consistency of different data sets is evident from the plots of apparent resistivities and phases in Fig. 11. A certain inconsistency between S and DP responses for the EEP data set follows from the discontinuous change of the slope of ϱ_a and the jump in the phase. This may indicate that the S responses plotted are not valid for such stable areas as the East European platform.

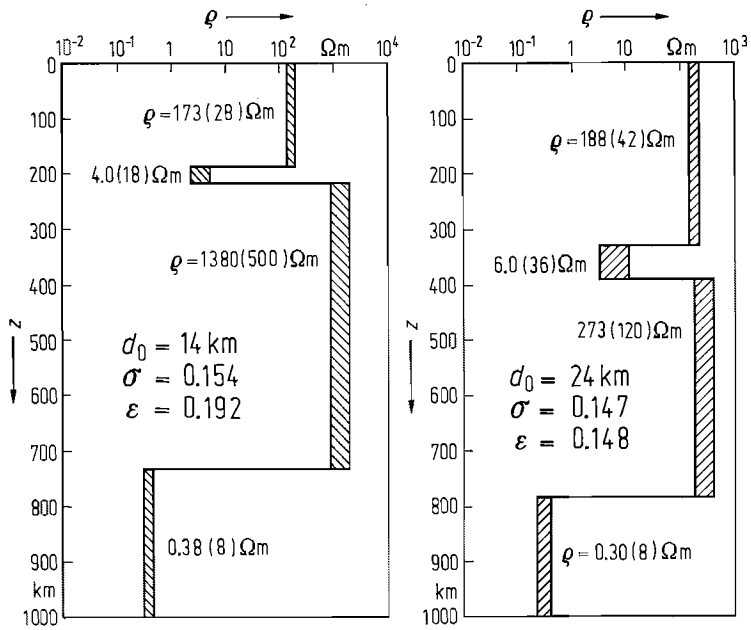

Fig. 9. 4-layer models for a combined interpretation of response estimates of Dst, S and DP variations. The estimates used are listed in Tables 6···9 under SCH-Y for Dst and S variations, in Tables 2···5 under SCA and NEW for DP variations. See also Fig. 10 for a $\varrho^*(z^*)$ diagram of the input data. In the model to the left DP responses from Scandinavia (SCA, periods 8200···890 s) are used, in the model to the right DP responses from Southern Scotland (NEW, periods 1961···585 s).

The combined interpretation requires the existence of a well conducting intermediate layer in the upper mantle with a conductance of 7500 and 10000 S, respectively. Note the resulting high mantle resistivities below this layer down to 7···800 km depth.

The numbers are the inferred layer resistivities in units of 1 Ωm with errors, d_0 is the layer parameter (from which the layer thickness can be found; cf. text), σ the rms error of the input logarithmic response $y(\omega)$, eq. (8), and ε the rms misfit between empirical and model responses, eq. (11).

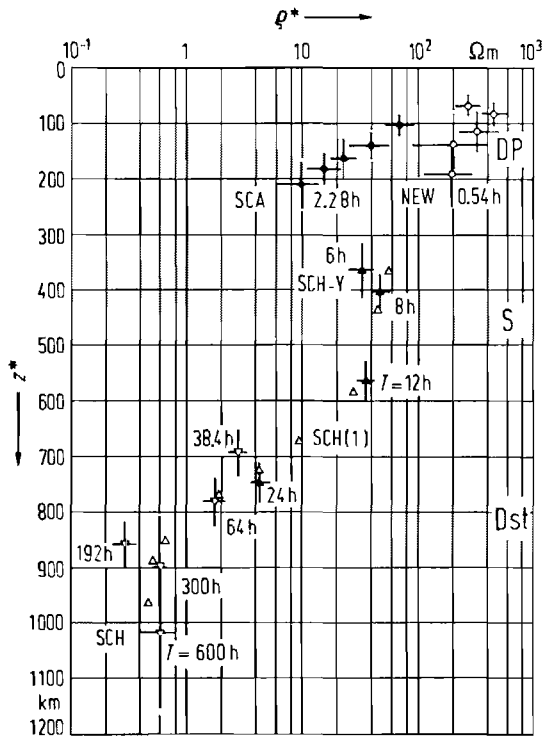

Fig. 10. Apparent resistivity $\varrho^*(z^*)$ diagram for solar daily variations S and smoothed storm-time variations Dst, derived with the $Z:Y$ method from a European network of inland observatories. For details, see subsect. 4.2.2.4.3. The response estimates displayed are listed in Tables 6···9 under SCH-Y. For comparison two sets of continental DP responses are added (SCA, NEW); see Fig. 5 for details. The numbers refer to the periods of individual estimates in units of 1 h. Open triangles without error bars mark theoretical Dst and S responses for model SCH(1) in Fig. 12, listed in Table 14.

The transition from high to low mantle resistivities between 600 and 800 km is evident from the steep reduction of ϱ^* values from about 40 Ωm to less than 1 Ωm. See Figs. 12···14 for models. Note the maximum and minimum ϱ^* values for 8 and 192 h at 400 and 850 km depth, respectively, which possibly indicate extremely high and low resistivities just above and below the transition. To obtain a smooth upward merging into the downgoing branches of the selected DP responses, an intermediate layer of low resistivity in the upper mantle is required. See the models in Fig. 9.

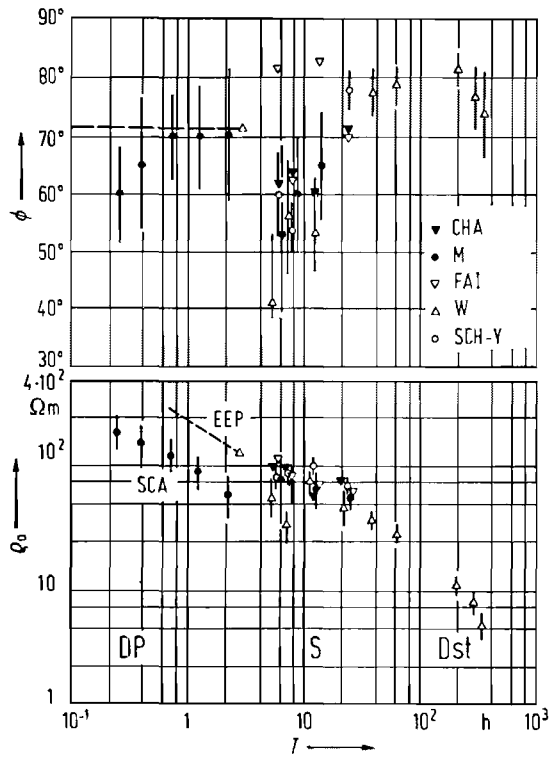

Fig. 11. Apparent resistivity ϱ_a and impedance phase ϕ for the four harmonics of diurnal S variations according to five different analyses. Extensions into adjoining period ranges are with Dst response estimates SCH-Y for Europe and with DP responses for Scandinavia (SCA) and the East-European Platform (EEP). See Tables 2, 4, 6, 8 for listed values. For Winch's analysis W, see Table 3 in subsect. 4.2.2. For EEP, see eq. (15) in the text.

Because the DP responses are from areas of low surface conductance and without crustal conductor, a nearly monotonic decrease of ϱ_a with period is observed and a phase well above 45 degrees. In the period range of S variations, however, ϱ_a is about stable and the phase drops from above 70 to below 65 degrees. Therefore the downward decrease in true mantle resistivity should be halted or even reversed within the upper mantle, leading to high resistivities in its lower part (cf. Fig. 9).

Figure 12 presents three models which can explain the S-Dst responses for the data set SCH-Y within their error limits. The theoretical responses for the first model SCH(1) are marked by triangles in the $\varrho^*(z^*)$ diagram of Fig. 10. The three models have comparable ε values, eq. (11), and thus explain the input responses equally well. Note that the mean rms error σ of the response estimates, defined as the harmonic mean of individual estimates for the nine periods involved, is slightly smaller then ε. This implies that the responses have still unused information, or that they are inconsistent. The second explanation is more likely. An obvious inconsistency exists, for instance, for the z^* value of the 24 h harmonic of S, which is greater than z^* of the 38.4 h period of Dst.

This attempt to interpret a specific set of S-Dst responses in the period range from 6 h to 20 d leads to the following conclusions: If a layered model is chosen, a subdivision into two layers and a uniform substratum is sufficient to explain this limited set of inaccurate data. Model SCH(1) has only three free parameters because the layer thicknesses have not been part of the fit by least-squares (cf. subsect. 2.3.1.3). One more layer in model SCH(2) improves the fit slightly, and the four layer resistivities are resolved within error limits. The improvement of the fit applies almost exclusively to the fourth S harmonic.

The resulting model SCH (2) is similar to those in Fig. 9 and thus can explain the response at shorter periods better than model SCH(1). In model SCH(3) an attempt is made to resolve a possible good conductor at the transition from the high resistivity to the low resistivity mantle at 800 km depth. Its presence is suggested by the closeness of the response estimates for 192 and 300 h, and the maximum phase for 192 h. Note that the response estimates ECK and BAN have also maximum phases for nearby periods (Table 8). As seen from Fig. 12 the expected resistivity minimum at 800 km is barely significant. The large number of subdivisions requires also the use of a generalized inverse method retaining only the three largest eigenvalues of the linear problem with nine adjustable parameters. Each layer resistivity thus represents an average over a number of adjacent layers according to eq. (10).

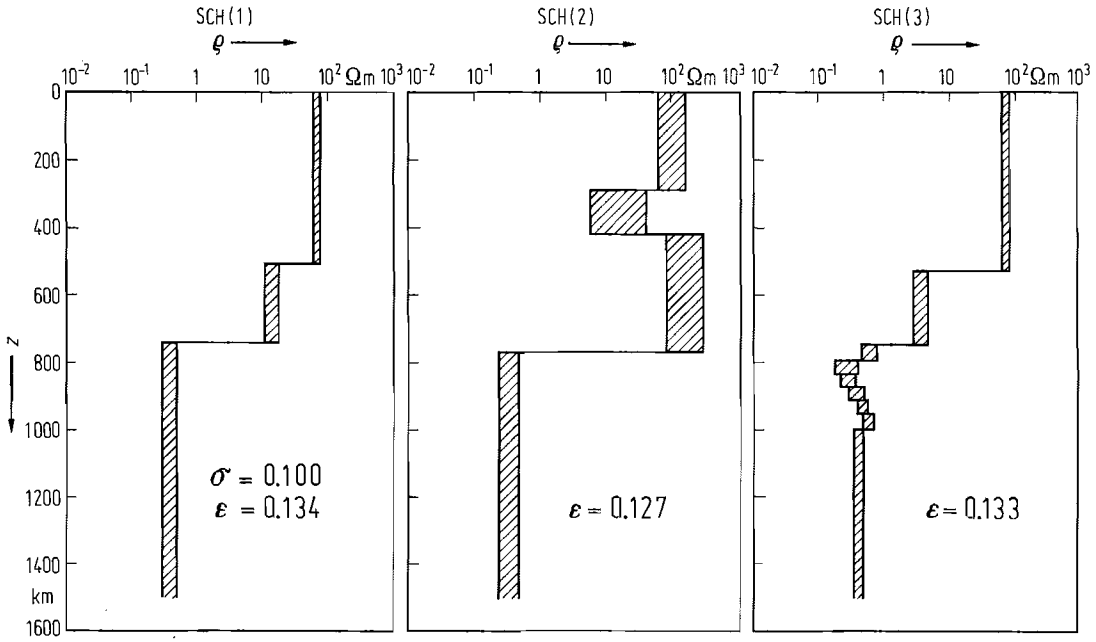

Fig. 12. Combined interpretation of diurnal S and Dst response estimates for Europe in the period range from 6 h to 20 days. Input data are nine logarithmic response estimates with the quoted rms error σ as listed under SCH-Y in Tables 6···10. Layer interfaces separate depth ranges for which mean values of the logarithmic resistivity are derived; hatching indicates their uncertainty.
The 3-layer model SCH(1) explains the input data almost within their error limits (see Fig. 10), i.e. the rms misfit ε of the logarithmic response (cf. eq. (11) exceeds only slightly the data rms error σ. The inclusion of more than three layers does not improve the fit to any extent, but resolves possible details of the mantle resistivity structure (cf. text).

In Fig. 13 model SCH (1) is compared with other models. To examine the influence of the choice of a specific data set, the various response estimates from Tables 6···9 for S and Dst variations are used as input data for the ψ-algorithm. In an arbitrary way, Malin's estimates for S were combined with Devane's estimates for Dst (M-DEV), Chapman's estimates for S with Banks' estimates for Dst (CHA-BAN). All models establish the mantle down to 500···600 km depth as a poor conductor with a mean resistivity between, say, 55 and 75 Ωm. The deviating value from Fainberg's responses is produced by their unrealistic high phases for the fourth and second harmonic of S (cf. Fig. 11). Note that the quoted mean value represents a geometric mean because the model parameter is the logarithm of the layer resistivity (cf. subsect. 2.3.3.3). In this way, none of the models is in conflict with those in Fig. 9. Below follows a thin layer with an intermediate resistivity around 10 Ωm, with a drop to about 0.5 Ωm at 700···800 km for the underlying half-space representing the low resistivity part of the mantle.

Two published models are added in Fig. 13 for comparison. Model BAN (2) is from Banks' interpretation of S and Dst responses [Ban72], R (3) is a layered approximation to an analytic model proposed by Rokityanski (cf. eq. (17)). In model BAN (2) the transition to low mantle resistivities occurs already between 500 and 600 km depth. This reflects the use of Banks' Dst continuum estimates which are inconsistent at high frequencies and thus biased toward lower mantle resistivities. Note that model CHA-BAN uses not Banks' continuum estimates, but his estimates for the 27 d periodicity and its subharmonics.

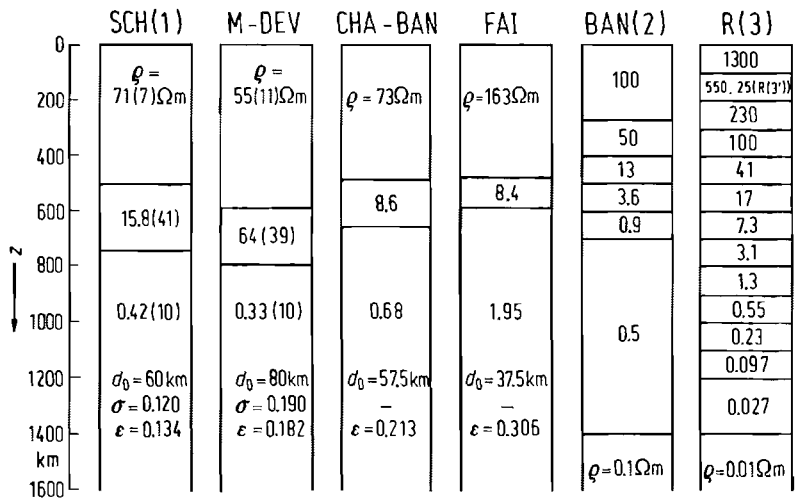

Fig. 13. Interpretation of global S and Dst response estimates by layered models. Numbers refer to layer resistivities in units of 1 Ωm. The models SCH(1) to FAI represent 3-layer models to interpret different combinations of response estimates listed in Tables 6···9 (cf. text); d_0 is the optimum layer parameter from which the layer thickness is to be derived, eq. (12), σ the rms data error, and ε the rms misfit, eq. (11).

The four models agree within error limits, where available. They place a transition layer of intermediate resistivity between the high and low resistivity mantle from 500··· 800 km depth. Note that ε increases from SCH(1) to FAI, which reflects the growing inconsistency of the input data. Model BAN(2) has been proposed by Banks on the basis of his own response estimates for the Dst continuum, model R(3) is a layered approximation to Rokityanski's semi-analytic model, eq. (17). In version R(3') it includes between 100 and 200 km depth a well conducting layer, proposed on the basis of other information.

As pointed out in subsect. 2.3.1.4, models with discontinuous changes of resistivities at layer boundaries can be equivalent within error limits to models with a continuous depth dependence of ϱ (cf. Fig. 1). For some simple analytic expressions of $\varrho(z)$ the response can be obtained in closed form and the parameter adjusted directly to the data. Various analytic model distributions of this kind have been proposed for combined S-Dst responses. Three of them are shown in Fig. 14 together with the 3-layer model SCH(1) from Fig. 12. Model LP(d) refers to the classical 2-parameter model of Lahiri and Price [Lah39], involving a power law increase of resistivity with geozentric distance:

$$\varrho(z)=\varrho_0\left(1-\frac{z}{R_E}\right)^n \quad \text{with } n=37, \text{ and } \varrho_0=250\,\Omega\text{m}. \tag{16}$$

To account for the 60° and 65° phases of, respectively, the second and third S harmonic (according to Chapman's analysis), Lahiri and Price had to include a thin surface shell with a conductance of 5100 S.

Rokityanski (subsection 4.5.4 in [Rok82]) adapted this model to a plane earth and proposed the model

$$\varrho(z)=\begin{cases}\varrho_0\exp(-l\,z/R_E), & z<z_H\\ \varrho_H, & z\geqq z_H\end{cases}$$

with

$$\varrho_0=2000\,\Omega\text{m}, \quad l=55$$
$$\varrho_H=0.01\,\Omega\text{m}, \quad z_H=1400\,\text{km}. \tag{17}$$

Figure 13 contains as model R(3) a 14 layer approximation. If in the second layer, from 100···200 km, the resistivity is lowered to 25 Ωm to simulate a good mantle conductor, model R(3') evolves which is identical with model "3(opt)" in Table 17 (p. 163) of [Rok82] except for some minor numerical discrepancies.

Model FAI(1) is the analytic model

$$\varrho(z)=\begin{cases}\varrho_0, & z<h_1\\ \varrho_0(z/h_1)^{-\gamma}, & z\geqq h_1\end{cases} \tag{18}$$

of Fainberg [Fai83]. It has three adjustable parameters which were adjusted to the S-Dst response after a transformation to a spherical earth with Weidelt's formula (eq. 3.6 in [Wei72]) for an unspecified degree n.

The resulting parameters are

$$\varrho_0=1.399\cdot10^{14}\,\Omega\text{m}, \quad \gamma=4.735.$$

No value has been assigned to h_1. In model FAI(1), $h_1=1$ km is used, disregarding the top layer. This reproduces the model shown in Fig. 6b of [Fai83]. As seen from Fig. 14 the three models are close to each other in the depth range from 400···1000 km, where the induction of S and Dst occurs. Hence, similar responses can be expected for these frequencies (cf. Tables 11···13).

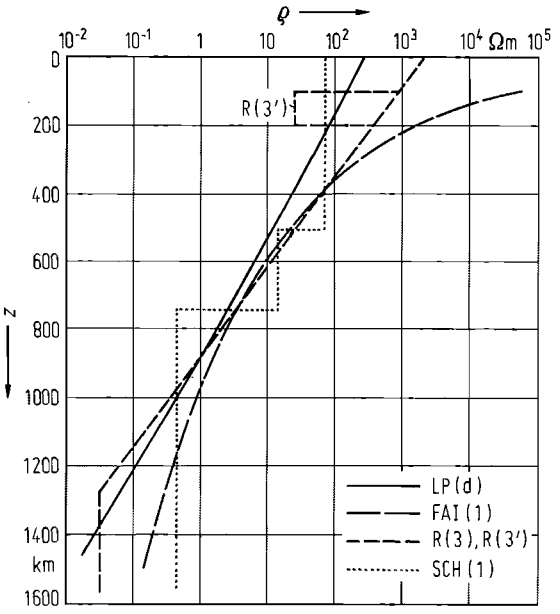

Fig. 14. Interpretation of global S and Dst responses by continuous resistivity models. LP(d): Lahiri and Price's model "d" for a spherical earth, eq. (16). R(3): Its adaption by Rokityanski for a plane earth, eq. (17). FAI(1): Fainberg's model, eq. (18). The 3-layer model SCH(1) from Fig. 12 is added for comparison. Theoretical responses for all models, including those for very short and very long periods, can be found in Tables 10···14.

Continuous models of this form are attractive when mantle resistivity is solely controlled by a smoothly increasing temperature and, possibly, pressure. See section 5.4 in [Ang82] for laboratory data on the temperature and pressure dependence of minerals and rocks which could be major constituents of the mantle. On the other hand, the deep mantle resistivity could be also controlled by more or less discontinuous phase or compositional changes, including partial melting, which would be better represented by a layered model.

Tables 10···13 list theoretical responses for the three models in Fig. 14. All of them reproduce the Dst response, but in the case of R(3) and FAI(1) large discrepancies are observed for the S response when compared with the empirical estimates in Table 6···9. These models are much too resistive in the mantle above 400 km and some good conductor at the surface or at shallow depth is needed to improve the fit. Model R(3') includes such conductor between 100 and 200 km and its response agrees better with the empirical estimates. This may be incidental, however, because model SCH(1) with a uniform mantle above 500 km gives equally close estimates.

The theoretical response values for layer model SCH(1) and the analytic models can be found in Tables 10···13. Note that the inclusion of a good conductor of 4000 S conductance within the top mantle changes the response of the entire period range of S variation as seen from a comparison of R(3) and R(3') responses. This conductor has about the same function as the surface layer of 5100 S in the LP(d) model to explain S and Dst responses with one model. Table 14 contains for models R(3) and R(3') theoretical responses at short periods. Use eq. (13), when, for known local conditions, a conducting surface layer is to be included.

Because Tables 10···13 include theoretical responses for the very long periods, the following conclusions can be drawn about lower mantle resistivities from a comparison with the empirical estimates in Tables 6···9: The 27 d periodicity has nearly the same response as the Dst continuum in the 20···25 d period range, which was part of all previous model adjustments. For annual variations, only one estimate is available and the source configuration is uncertain. For these long periods, the C_n response depends also on the degree n. Hence, all inferences of deep mantle resistivities rely on the 11-year solar cycle variations:

The three listed estimates agree in $z^* = \mathrm{Re}\{C_n\}$, but disagree in phase. Of the models, R(3) gives a too shallow penetration depth z^*, model SCH(1) a too large one, while model FAI(1) is about right. Model FAI(1) also gives a phase of 79.8° which lies about halfways between the phase estimates of Harwood and Ducruix. Hence, this model appears to be the best approximation to the lower mantle resistivity down to about 2000 km depth, the penetration depth of solar cycle variations, where it reaches 0.033 Ωm.

This value is in agreement with estimates for the lower mantle from upward diffusing secular variations of the earth's main field [McD57]. The time and space dependence of secular variations as observed at the earth's surface puts a definite lower limit to the mean mantle resistivity. Elsasser's classical estimate was 0.02 Ωm; Ducruix et al. [Duc80], on the basis of recently observed almost discontinuous changes of secular variations, so-called "jerks", allow for the lower mantle a resistivity as low as 0.01 Ωm, including all available information about mantle resistivities above 1000 km depth.

Table 10. Theoretical responses Q_n and C_n for the spherical 3-layer earth model SCH (1) in Fig. 13, and the zero-wavenumber response C_0 for the equivalent plane earth model. The apparent resistivities ϱ_a, ϱ^*, and the phase ϕ refer to the spherical model.

Variation	T	n	Q_n 10^{-3}	C_n km	C_0 km	ϱ_a Ωm	ϕ degree	ϱ^* Ωm
S	6 h	5	385+208i	375−248i	372−281i	73.8	56.6	44.8
	8 h	4	388+178i	439−261i	442−292i	71.5	59.3	37.3
	12 h	3	386+135i	532−259i	541−284i	64.0	64.1	24.5
	24 h	2	376+ 77i	660−214i	673−229i	44.0	72.0	8.40
Dst	1.6 d	1	346+ 36i	723−187i	729−192i	31.9	75.5	4.01
	2.7 d	1	339+ 31i	765−163i	772−168i	21.0	78.0	1.82
	8.0 d	1	324+ 31i	843−167i	852−174i	8.4	78.8	0.64
	12.5 d	1	317+ 34i	880−189i	890−197i	5.9	77.9	0.52
	25.0 d	1	303+ 43i	953−244i	965−256i	3.5	75.7	0.43
Very long period	27 d	1	302+ 45i	963−251i		3.35	75.4	0.43
	1 a	2	90+116i	1629−511i		0.730	72.6	0.13
	11 a	1	6+ 39i	3111−365i		0.223	83.3	0.006

Table 11. Theoretical response C_n for the spherical analytic earth models of Rokityanski R(3), R(3′) and Fainberg FAI(1) in eqs. (17) and (18), respectively, see also Fig. 13 and Fig. 14 for model R(3′).

T h	n	C_n km		
		FAI(1)	R(3)	R(3′)
6 h	5	543−108i	529−135i	371−219i
8 h	4	578−121i	568−145i	424−235i
12 h	3	625−136i	620−155i	502−247i
24 h	2	703−159i	705−165i	630−245i
1.6 d	1	765−179i	768−174i	714−241i
2.7 d	1	825−191i	825−174i	791−226i
8.0 d	1	970−219i	947−173i	934−199i
12.5 d	1	1036−235i	998−172i	990−191i
25.0 d	1	1134−227i	1074−164i	1069−176i
27 d	1	1145−237i	1081−164i	1078−174i
1 a	2	1518−271i	1257−148i	1262−149i
11 a	1	2214−398i	1686−407i	1686−407i

Table 12. Theoretical response Q_n for spherical analytic earth models. See legend to Table 11 for explanations.

T	n	Q_n 10^{-3}		
		FAI(1)	R(3)	R(3′)
6 h	5	281+76i	288+97i	395+186i
8 h	4	317+73i	321+89i	403+163i
12 h	3	349+67i	350+76i	403+132i
24 h	2	363+56i	362+58i	386+ 89i
1.6 d	1	338+34i	338+33i	347+ 46i
2.7 d	1	327+35i	327+32i	333+ 42i
0.8 d	1	301+39i	305+31i	307+ 36i
12.5 d	1	289+39i	296+30i	297+ 34i
25.0 d	1	272+40i	283+28i	284+ 30i
27 d	1	270+40i	282+28i	282+ 30i
1 a	2	125+65i	194+40i	192+ 40i
11 a	1	111+52i	183+60i	183+ 60i

Table 13. Apparent resistivities ϱ_a, ϱ^*, and impedance phase ϕ for spherical analytic earth models; see legend to Table 11 for explanations.

T	n	ϱ_a Ωm			ϕ degree			ϱ^* Ωm		
		FAI(1)	R(3)	R(3′)	FAI(1)	R(3)	R(3′)	FAI(1)	R(3)	R(3′)
6 h	5	112	109.2	67.9	78.7	75.7	61.0	8.56	13.4	35.1
8 h	4	95.6	94.2	64.4	78.1	75.7	59.4	8.02	11.5	30.3
12 h	3	74.7	74.7	57.1	77.7	76.0	63.8	6.80	8.8	22.3
24 h	2	47.4	47.8	41.8	77.3	76.9	68.8	4.62	4.9	10.9
1.6 d	1	35.3	35.4	32.5	76.8	77.2	71.3	3.67	3.5	6.65
2.7 d	1	24.6	24.4	23.2	76.9	78.1	74.1	2.51	2.1	3.49
8.0 d	1	11.3	10.6	10.4	77.3	79.6	78.0	1.10	0.69	0.91
12.5 d	1	8.22	7.50	7.43	77.7	80.2	79.1	0.75	0.43	0.53
25 d	1	4.91	4.31	4.29	78.3	81.3	80.7	0.40	0.20	0.23
27 d	1	4.62	4.04	4.03	78.3	81.4	80.8	0.38	0.18	0.21
1 a	2	0.595	0.401	0.404	79.9	83.3	83.3	0.037	0.011	0.011
11 a	1	0.115	0.069	0.069	79.8	76.4	76.4	0.0072	0.0076	0.0076

Table 14. Theoretical zero-wavenumber response C_0, apparent resistivities ϱ_a and ϱ^*, and phase ϕ of the impedance for Rokityanski's models R(3) and R(3') in Fig. 13, calculated for a plane earth and the period range of polar substorm variations. First value: model R(3') with conducting upper mantle layer from 100 to 200 km; second value: model R(3) without this layer.

T s	C_0 km		ϱ_a Ωm		ϕ degree		ϱ^* Ωm	
	R(3')	R(3)	R(3')	R(3)	R(3')	R(3)	R(3')	R(3)
14400	299 − 219 i	519 − 169 i	75.6	163	53.7	71.9	52.8	31.4
7200	210 − 157 i	444 − 163 i	75.5	246	53.3	69.8	54.0	58.4
3600	163 − 100 i	372 − 155 i	80.0	356	58.6	67.4	43.5	105
1800	141 − 61 i	304 − 144 i	104	496	66.5	64.7	33.0	181
900	130 − 41 i	242 − 129 i	163	658	72.4	61.9	29.9	293
450	121 − 33 i	187 − 113 i	274	836	74.6	59.0	38.8	444

2.3.1.8 The resistivity of crust and mantle beneath oceans

Present knowledge about the crustal and upper mantle resistivity beneath oceans comes almost exclusively from magnetotelluric seafloor observations in the North Pacific. See [Fil73] and [Fil80a] for instrumental techniques which have been developed by the cited author to record geomagnetic and telluric time variations at the bottom of deep oceans. Land-based geomagnetic observations along coastlines and on islands provide additional information through the coast and island effects. See subsect. 2.3.2 for details. The principles of seafloor electromagnetic studies can be found in [Cox71] and [Cox80b]. The special problem of crustal investigations, which arise from the screening effect of the seawater on fast geomagnetic variations, is dealt with in [Cox81].

When compared to land-based observations, magnetotelluric seafloor experiments offer various advantages:

(i) Stray fields from artificial sources are virtually absent; in particular the noise level of the telluric field is exceptionally low and - apart from instrumental noise - determined by motion-induced electric fields. This allows the record of low amplitude, low frequency telluric variations connected to smoothed storm-time geomagnetic variations Dst.

(ii) The oceanic lithosphere is exposed to magnetotelluric soundings with a minimum of screening and telluric distortion by conducting sediments at the sea bottom. This removes the major obstactle for deep magnetotelluric studies on land, where the great complexity of surficial layers reflects with strong resistivity contrasts the accumulated geological record of the earth's history since Precambrian times.

(iii) Motion-induced electric fields arise at the ocean floor from long-period barotropic waves, internal waves and tidal currents which move sea water across field lines of the earth's planetary magnetic field. Even though this complicates the analysis of seafloor telluric records, it can add also knowledge on deep resistivity where concurrent oceanographic observations allow a sufficiently detailed description of the water motion. See the cited sources for techniques to separate motion-induced and electromagnetically induced telluric fields. See also subsect. 4.2.2 on this subject.

Electromagnetic screening by the conducting ocean water limits the period range for seafloor studies with variation fields of external origin. In detail: The resistivity of saltwater at 2 °C is $\varrho_{sw}=0.31$ Ωm (see also [Ang82]), giving 4.5 km deep oceans a conductance of 14000 S. The skin depth value of sea water at period T in [s] is $p(T)=\sqrt{\varrho_{sw}\,T/\pi\mu_0}=0.28\sqrt{T}$ km, which implies that geomagnetic pulsations with periods up to $T=300$ s and $p\approx 4.5$ km are practically shielded from the bottom by induced eddy currents in the ocean.

For longer periods the screening depends also on the resistivity distribution below the seafloor. But note that any high resistivity portion of the oceanic crust or mantle will be hardly distinguishable from a non-conductor. For seafloor magnetotelluric soundings with fields of external origin the limitations of example (3), subsect. 2.3.1.4, apply with respect to the maximum resolvable resistivity ϱ_T of intermediate layers of high resistivity between good conductors. Because of the quoted high conductance of oceans, even moderately resistive layers may have an unresolvable finite resistivity. Therefore alternative methods are developed currently to investigate the resistivity in the oceanic crust, in particular active electromagnetic methods with transmitter and receivers placed on the seafloor [Cox81].

Since nothing is known presently about in-situ resistivities directly beneath the seafloor, the following estimates for a typical oceanic crust are from laboratory data, seismic data, and petrological models [Cox81]: Below the sea water with the quoted mean resistivity (mean depth of ocean basins: 4.5 km) and usually not more than 500 m of water saturated bottom sediments with 0.5 to 1 Ωm follows, as layer "2", roughly 2 km of basalt. In

Table 14. Theoretical zero-wavenumber response C_0, apparent resistivities ϱ_a and ϱ^*, and phase ϕ of the impedance for Rokityanski's models R(3) and R(3') in Fig. 13, calculated for a plane earth and the period range of polar substorm variations. First value: model R(3') with conducting upper mantle layer from 100 to 200 km; second value: model R(3) without this layer.

T s	C_0 km		ϱ_a Ωm		ϕ degree		ϱ^* Ωm	
	R(3')	R(3)	R(3')	R(3)	R(3')	R(3)	R(3')	R(3)
14400	299 − 219 i	519 − 169 i	75.6	163	53.7	71.9	52.8	31.4
7200	210 − 157 i	444 − 163 i	75.5	246	53.3	69.8	54.0	58.4
3600	163 − 100 i	372 − 155 i	80.0	356	58.6	67.4	43.5	105
1800	141 − 61 i	304 − 144 i	104	496	66.5	64.7	33.0	181
900	130 − 41 i	242 − 129 i	163	658	72.4	61.9	29.9	293
450	121 − 33 i	187 − 113 i	274	836	74.6	59.0	38.8	444

2.3.1.8 The resistivity of crust and mantle beneath oceans

Present knowledge about the crustal and upper mantle resistivity beneath oceans comes almost exclusively from magnetotelluric seafloor observations in the North Pacific. See [Fil73] and [Fil80a] for instrumental techniques which have been developed by the cited author to record geomagnetic and telluric time variations at the bottom of deep oceans. Land-based geomagnetic observations along coastlines and on islands provide additional information through the coast and island effects. See subsect. 2.3.2 for details. The principles of seafloor electromagnetic studies can be found in [Cox71] and [Cox80b]. The special problem of crustal investigations, which arise from the screening effect of the seawater on fast geomagnetic variations, is dealt with in [Cox81].

When compared to land-based observations, magnetotelluric seafloor experiments offer various advantages:

(i) Stray fields from artificial sources are virtually absent; in particular the noise level of the telluric field is exceptionally low and - apart from instrumental noise - determined by motion-induced electric fields. This allows the record of low amplitude, low frequency telluric variations connected to smoothed storm-time geomagnetic variations Dst.

(ii) The oceanic lithosphere is exposed to magnetotelluric soundings with a minimum of screening and telluric distortion by conducting sediments at the sea bottom. This removes the major obstactle for deep magnetotelluric studies on land, where the great complexity of surficial layers reflects with strong resistivity contrasts the accumulated geological record of the earth's history since Precambrian times.

(iii) Motion-induced electric fields arise at the ocean floor from long-period barotropic waves, internal waves and tidal currents which move sea water across field lines of the earth's planetary magnetic field. Even though this complicates the analysis of seafloor telluric records, it can add also knowledge on deep resistivity where concurrent oceanographic observations allow a sufficiently detailed description of the water motion. See the cited sources for techniques to separate motion-induced and electromagnetically induced telluric fields. See also subsect. 4.2.2 on this subject.

Electromagnetic screening by the conducting ocean water limits the period range for seafloor studies with variation fields of external origin. In detail: The resistivity of saltwater at 2 °C is $\varrho_{sw}=0.31$ Ωm (see also [Ang82]), giving 4.5 km deep oceans a conductance of 14000 S. The skin depth value of sea water at period T in [s] is $p(T)=\sqrt{\varrho_{sw}\,T/\pi\mu_0}=0.28\sqrt{T}$ km, which implies that geomagnetic pulsations with periods up to $T=300$ s and $p\approx 4.5$ km are practically shielded from the bottom by induced eddy currents in the ocean.

For longer periods the screening depends also on the resistivity distribution below the seafloor. But note that any high resistivity portion of the oceanic crust or mantle will be hardly distinguishable from a non-conductor. For seafloor magnetotelluric soundings with fields of external origin the limitations of example (3), subsect. 2.3.1.4, apply with respect to the maximum resolvable resistivity ϱ_T of intermediate layers of high resistivity between good conductors. Because of the quoted high conductance of oceans, even moderately resistive layers may have an unresolvable finite resistivity. Therefore alternative methods are developed currently to investigate the resistivity in the oceanic crust, in particular active electromagnetic methods with transmitter and receivers placed on the seafloor [Cox81].

Since nothing is known presently about in-situ resistivities directly beneath the seafloor, the following estimates for a typical oceanic crust are from laboratory data, seismic data, and petrological models [Cox81]: Below the sea water with the quoted mean resistivity (mean depth of ocean basins: 4.5 km) and usually not more than 500 m of water saturated bottom sediments with 0.5 to 1 Ωm follows, as layer "2", roughly 2 km of basalt. In

its upper portion pillow basalt and submarine lava flows will have sufficiently connected fissures filled with sea water to lower the overall resistivity to, say, 30 Ωm as a geometric mean. The lower portion, containing more compact material including feeder dykes, may be more resistive. The same should apply to the 4 km of layer "3" of the oceanic crust. It may have the resistivity, above 1000 Ωm, of cooled down dry igneous rocks where the crust is old, but should be with, say, 10 Ωm less resistive where the crust is young, hot and with circulating water. So far there is no direct evidence, however, that the lower oceanic crust at or near midocean ridges contains such good conductors or that there are interspersed deep crustal conductors at all as they exist in the continental crust (cf. subsect. 2.3.1.6).

Magnetotelluric seafloor response estimates from three sites in the North Pacific are assembled in Fig. 15 and the Tables 15···18. For not included published soundings at four more sites in the Pacific, see [Fil81]. For the only seafloor experiment in the Atlantic, see [Cox80a].

This total number of eight seafloor experiments and one island experiment, covering the period range from about 5 min to 2 d, suggest the following: Magnetotelluric soundings at EPR and MIA set in at periods of 5 to 10 min with a depth of penetration z^* of 25 to 30 km. In contrast to land-based observations (Fig. 5), apparent resistivities ϱ^* for this depth are close to each other with a tendency that the uppermost mantle is less resistive beneath ocean ridges (EPR) than away from them (MIA). They range from 40 Ωm at EPR to 140 Ωm at MIA for the quoted subcrustal depth (Table 16), increasing to 60 Ωm and more than 300 Ωm for $z^* \approx 50$ km. A corresponding rise in true resistivity within the uppermost mantle is seen in the top layers of the models in Fig. 16. Note that phase estimates from the quoted Mariana sounding are well below 45 degrees (Table 17), i.e. no evidence exists for any high resistivity crustal layer as proposed in the above conjectures for old sections of the seafloor.

At periods close to 30 min maximum apparent resistivities ϱ^* between 50 and 100 km in z^* are modelled by the beginning of the most resistive part of the upper mantle at 70 km depth (Fig. 16) with true resistivities of 500 Ωm for MIA and 75 Ωm for EPR. Soundings at other seafloor sites do not require such detailed uppermost mantle structure and suggest an overall resistivity of 100 to 1000 Ωm. See model HAW in Fig. 16 and the collection of models in [Fil82a], Fig. 8 cited in subsect. 4.2.2.5.

For periods between one hour and two days, so far the longest resolved period in magnetotelluric seafloor studies, a generally smooth decrease of apparent resistivity ϱ^* with period and thereby penetration depth z^* is observed. Note in Fig. 15, the displacement of the sounding profiles $\varrho^*(z^*)$ against each other according to crustal age, implying that the most resistive mantle is found beneath old sections of oceanic lithosphere and the least resistive mantle beneath young sections. The transition from high resistivity (> 50 Ωm) to low resistivity (< 5 Ωm) mantle is shifted in the models of Fig. 16 from 300 km beneath the Eastern Pacific rise (EPR) to 650 km beneath one of the oldest crustal sections of the Pacific (MIA).

There are no clear indications of an intermediate good conductor in the upper mantle with a subsequent rise in resistivity towards greater depth. Only the model for the Hawaiian island data (OAH) includes a conducting layer at 350 km depth. Models for two North Pacific soundings between Hawaii and the Californian coast, crustal age 30 and 72 million years, respectively, propose also such mantle conductors for 150 and 100 km depth, respectively [Fil80b]. A comparison of oceanic and continental response estimates for long periods (Figs. 10 and 15) shows some similarity where the oceanic crust is old. Note the difference in overall mantle resistivity down to 500 km depth: 70 Ωm in model SCH(1) of Fig. 13 for continents, but 500 Ωm in model MIA of Fig. 16 for an old section of the ocean. Otherwise the oceanic upper mantle from, say, 100 km to 500 km depth appears as less resistive than the upper mantle beneath continents.

No seafloor response estimates are known for periods beyond 2 days in period, which leaves the deep mantle resistivity uncertain. Individual response estimates at very long periods for a land-based global network of observatories listed in Table 5 of subsect. 4.2.2 suggest a laterally uniform deeper mantle when the penetration depth reaches, with few exceptions, uniformly 1000 km for continental, coastal, and island observatories.

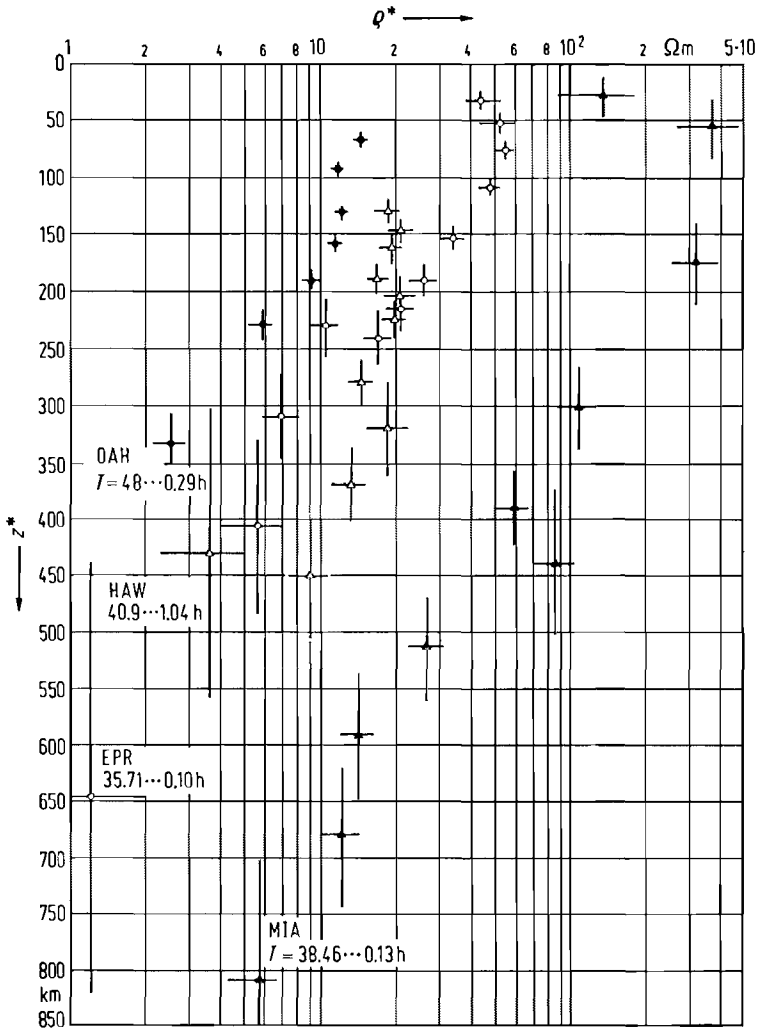

Fig. 15. Apparent resistivity $\varrho^*(z^*)$ diagrams for magnetotelluric studies in oceans. MIA: Seafloor sounding in the forearc basin of the Mariana island, crustal age $160 \cdot 10^6$ a. HAW: Seafloor sounding northeast of the Hawaiian islands, crustal age $50 \cdots 70 \cdot 10^6$ a. EPR: Seafloor sounding on the Eastern Pacific Rise, crustal age $4 \cdot 10^6$ a. OAH: Island sounding in Oahu, Hawaiian island. See Table 12 of subsect. 4.2.2 for details on the data source and for the periods of individual estimates. Numbers below site symbols give the period range displayed. – Soundings MIA and EPR indicate an increase of resistivity with depth within the uppermost mantle. Otherwise a smooth decrease of ϱ^* with increasing period and penetration depth z^* is observed, implying a corresponding reduction of true mantle resistivity. See Fig. 16 for models, and note that the transition from high to low resistivity in the mantle moves upward with decreasing crustal age.

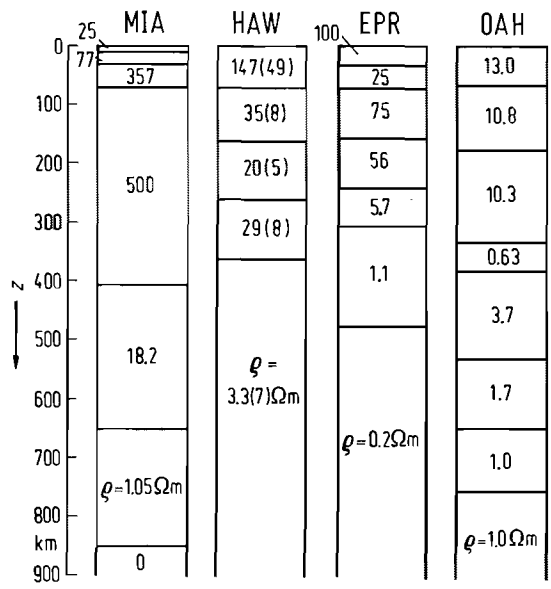

Fig. 16. Layered resistivity models from the quoted sources in Table 12, subsect. 4.2.2, to interpret the response data shown in Fig. 15. The numbers give the layer resistivities in units of 1 Ωm. See also Tables 15···18 for a list of input data. In the case of model EPR the proposed 7-layer model was selected.

Table 15. Apparent resistivity ϱ_a derived from the magnetotelluric impedance at seafloor and island sites. The evaluated impedance estimates are listed and explained in Table 12 of subsect. 4.2.2. * means a combined estimate from two or three listed values at adjacent frequencies.

T h	ϱ_a Ωm			
	MIA	HAW	EPR	OAH
38···48	40(8)	11(5)	26(15)	6.2(9)
16···18	68(9)	30(5)	24(7)	10.7(7)
8···10	85(12)	38(4)	30(5)	13.1(6)
6···7	101(13)	43(7)		14.0(5)
4···5.9	130(21)	43(4)*	30(4)	13.6(4)*
3···3.9	135(18)	41(4)	46(6)	11.8(3)*
2.5···2.9		42(5)	54(6)	9.8(2)*
2.0···2.4		44(3)*		9.0(2)*
1.5···1.9	190(26)	43(4)*	51(4)	
1.25···1.49		45(4)*	58(4)	
0.9···1.2		44(5)*	59(3)	
0.5···0.8	244(44)		56(5)	
0.2···0.3	133(38)		58(10)	
0.1···0.15	60(21)		49(9)	

Table 16. Modified apparent resistivity ϱ^* from magnetotelluric soundings at seafloor and island sites. See legend to Table 15 for further explanations.

T h	ϱ^* Ωm			
	MIA	HAW	EPR	OAH
38···48	5.4(12)	3.6(13)	1.2(7)	2.5(4)
16···18	12.0(16)	9.0(15)	5.5(15)	5.9(4)
8···10	13.9(20)	13.4(13)	7.0(11)	9.3(4)
6···7	26.1(32)	18.6(32)		11.4(4)
4···5.9	82.7(133)	14.6(13)*	10.4(15)	12.2(3)*
3···3.9	59.4(77)	20.5(18)	17.0(22)	11.6(2)*
2.5···2.9		20.8(23)	21.0(21)	14.8(3)*
2.0···2.4	108(15)	17.0(13)*		(390)*
1.5···1.9		19.5(17)*	26.3(21)	
1.25···1.49		20.9(18)*	33.8(22)	
0.9···1.2		19.0(17)*	48.7(27)	
0.5···0.8	318(57)		55.8(55)	
0.2···0.3	372(107)		52.1(86)	
0.1···0.15	136(48)		44.7(81)	

Table 17. Phase ϕ of the impedance from magnetotelluric soundings at seafloor and island sites. See legend to Table 15 for further explanations.

T h	ϕ degree			
	MIA	HAW	EPR	OAH
38···48	75(7)	66(11)	81(17)	63(4)
16···18	73(4)	67(5)	70(8)	58(2)
8···10	73(4)	65(3)	70(5)	53(1)
6···7	69(4)	62(5)		50(1)
4···5.9	56(5)	66(3)*	65(4)	48(1)*
3···3.9	62(4)	60(3)	65(4)	45(1)*
2.5···2.9		60(3)	64(3)	35(1)*
2.0···2.4	58(4)	64(3)*		(12)*
1.5···1.9		62(3)*	60(2)	
1.25···1.49		61(3)*	57(2)	
0.9···1.2		62(3)*	50(2)	
0.5···0.8	38(8)		45(3)	
0.2···0.3	25(8)		48(5)	
0.1···0.15	28(10)		48(5)	

Table 18. Depth z^* of perfect substitute conductor derived from the magnetotelluric impedance at seafloor and island sites. See legend to Table 15 for further explanations.

T h	z^* km			
	MIA	HAW	EPR	OAH
38···48	810(110)	430(125)	650(210)	330(28)
16···18	680(60)	450(50)	410(80)	238(9)
8···10	590(60)	370(30)	310(40)	193(6)
6···7	530(50)	320(40)		161(3)
4···5.9	440(60)	282(18)	231(22)	129(2)
3···3.9	390(40)	224(16)	243(23)	96(2)
2.5···2.9		204(18)	230(18)	69(1)
2.0···2.4		191(11)		(20)
1.5···1.9	305(34)	163(11)	185(12)	
1.25···1.49		147(9)	156(8)	
0.9···1.2		131(10)	119(6)	
0.5···0.8	176(36)		81(8)	
0.2···0.3	56(25)		53(8)	
0.1···0.15	28(14)		34(6)	

2.3.1.9 References for 2.3.1

2.3.1.9.1 Monographs and collections of review articles

Ada76 Adam, A. (ed): Geoelectric and geothermal studies, KAPG Geophysical monograph. Budapest: Akademiai Kiado **1976**.

Cox71 Cox, C.S., Filloux, J.H., Larsen, J.C.: Electromagnetic studies of ocean currents and electrical conductivity below the ocean-floor. In: A. Maxwell (ed.), The Sea, New York: Wiley, Vol. **4**, part 1 (1971) pp. 637–693.

Kel81 Kaufmann, A.A., Keller, G.V.: The magnetotelluric sounding method. Amsterdam-Oxford-New York: Elsevier **1981**.

Koe79 Koefoed, O.: Geosounding principles. Vol. 1: Resistivity sounding measurements. Amsterdam-Oxford-New York: Elsevier **1979**.

Pat80 Patra, H.P., Mallick, K.: Geosounding principles. Vol. 2: Time-varying geoelectric soundings. Amsterdam-Oxford-New York: Elsevier **1979**.

Por75 Porstendorfer, G.: Principles of magneto-telluric prospecting. Berlin, Stuttgart: Bornträger **1975**.

Rok82 Rokityansky, I.I.: Geoelectromagnetic investigation of the earth's crust and mantle. Berlin, Heidelberg, New York: Springer **1982**.

Sch80 Schmucker, U. (ed.): Electromagnetic induction in the earth and moon. J. Geomagn. Geoelectr. **32** (1980) Suppl. I.

Wai82 Wait, J.R.: Geo-Electromagnetism. New York-London: Academic Press **1982**.

Collective review papers presented at the IAGA Workshops on electromagnetic induction in the earth and moon

1972 Phys. Earth Planet. Inter. **7** (1973) No. 3.

1974 Phys. Earth Planet. Inter. **10** (1975) No. 3.

1976 Acta Geodet. Geophys. Montanist. **11** (1976) Nos. 3–4; **12** (1976) Nos. 1–3.

1978 Geophys. Surveys **4** (1980) Nos. 1 and 2.

1980 Geophys. Surveys **4** (1982) 331.

1982 Geophys. Surveys **6** (1983) 1.

2.3.1.9.2 Special references

Ang82 Angenheister, G. (ed.): Landolt-Börnstein, NS vol. V/1b: Physical properties of rocks. Berlin-Heidelberg-New York: Springer **1982**.

Bai70 Bailey, R.C.: Proc. R. Soc. London A **315** (1970) 185.

Ban72 Banks, R.J.: J. Geomagn. Geoelectr. **24** (1972) 337.

Blo77 Blohm, E.K., Worzyk, P., Scriba, H.: J. Geophys. **43** (1977) 665.

Blo80 Blohm, E.K., Homilius, J.: Geol. Jahrb. Reihe E **19** (1980) 39.

Cox80a Cox, C.S., Filloux, J.H., Gough, D.I., Larsen, J.C., Poehls, K.A., Von Herzen, R.P., Winter, R.: J. Geomagn. Geoelectr. **32**, Suppl. I (1980) S I 13.

Cox80b Cox, C.S.: Geophys. Surv. **4** (1980) 137.

Cox81 Cox, C.S.: Phys. Earth Planet. Inter. **25** (1981) 196.

Dub82 Duba, A.G., Shankland, T.J.: Geophys. Res. Letters **9** (1982) 1271.

Duc80 Ducruix, J., Courtillot, V., Le Mouël, J.-L.: Geophys. J. R. Astron. Soc. **61** (1980) 73.

Fai78 Fainberg, E.B., Sidorov, V.A.: Total conductivity of the sedimentary cover and watershell of the earth. IZMIRAN Akad. Nauka, Moscow (1978).

Fai83 Fainberg, E.B.: Global geomagnetic sounding. Preprint No. 50a. Institute of Terrestrial Magnetism, Ionosphere and Radiowave Propagation, Academy of Sciences of the USSR, Moscow (1983).

Fil73 Filloux, J.H.: Phys. Earth Planet. Inter. **7** (1973) 323.

Fil80a Filloux, J.H.: J. Geomagn. Geoelectr. **32**, Suppl. I (1980) SI 1.

Fil80b Filloux, J.H.: Earth Planet. Sci. Lett. **46** (1980) 244.

Fil81 Filloux, J.H.: Phys. Earth Planet. Inter. **25** (1981) 187.

Joe83 Jödicke, H., Untiedt, J., Olgemann, W., Schulte, L., Wagenitz, V.: Electrical conductivity structure of the crust and upper mantle beneath the Rhenish Massif, in: K. Fuchs et al. (eds.) Plateau Uplift. Berlin, Heidelberg, New York: Springer **1983**.

Jon82 Jones, A.: Tectonophysics **90** (1982) 37.

Jon83 Jones, A.G.: J. Geophys. **53** (1983) 72.

Kai83 Kaikkonen, P., Vanyan, L.L., Hjelt, S.E., Shilovsky, A.P., Pajunpää, K., Shilovsky, P.P.: Phys. Earth Planet. Inter. **32** (1983) 301.
Kar82 Kariya, K.A., Shankland, T.J.: Interpretation of electrical conductivity in the lower crust. Los Alamos Nat. Lab. Manuscript LA-9050-MS (1982).
Kar83 Kariya, K.A., Shankland, T.J.: Geophysics **48** (1983) 52.
Lah39 Lahiri, B.N., Price, A.T.: Phil. Trans. R. Soc. London **A 237** (1939) 509.
Lar75 Larsen, J.C.: Geophys. J. R. Astron. Soc. **43** (1975) 17.
McD57 McDonald, K.L.: J. Geophys. Res. **62** (1957) 117.
Par82 Parker, R.L.: Geophys. J. R. Astron. Soc. **68** (1982) 165.
Van77 Vanyan, L.L., Berdichevski, M.N., Fainberg, E.B., Fiskina, M.V.: Phys. Earth Planet. Inter. **14** (1977) P1.
Van80 Vanyan, L.L.: Progress report on ELAS-project. IAGA News **19** (1980).
Vzi78 Van Zijl, J.S.V.: Trans. Geol. Soc. S. Afr. **81** (1978) 129.
Vla72 Vladimirov, N.P., Dmitriev, V.I.: Geoelectric profile of the earth's crust and upper mantle on the territory of the Russian platform according to the data of magneto telluric sounding. Izv. Akad. Nauk SSSR, Fiz. Zemli **6** (1972) 100.
Wei72 Weidelt, P.: Z. Geophys. **38** (1972) 257.
Wig72 Wiggins, R.A.: Rev. Geophys. Space Phys. **10** (1972) 251.

2.3.2 Anomalies of the electrical conductivity in the earth's crust and upper mantle

2.3.2.0 List of symbols

$A(\omega)$, $B(\omega)$	transfer functions relating Z to H and D, respectively
$\overline{AB}$	current electrode distance (Schlumberger method)
$\boldsymbol{B}$	magnetic field vector (induction), in [nT]
D	magnetic East component of $\boldsymbol{B}$, in [nT]
$\boldsymbol{e}_D$, $\boldsymbol{e}_H$	(horizontal) unit vectors pointing to magnetic East and North, respectively
H	magnetic North component of $\boldsymbol{B}$, in [nT]
$\vec{P}$, $\vec{Q}$	induction arrows related to real and imaginary part of transfer function, respectively, eq. (3)
$\vec{P}_\mathrm{P}$, $\vec{Q}_\mathrm{P}$	induction arrows with Parkinson's direction definition adopted, direction opposite to $\vec{P}_\mathrm{W}$ and $\vec{Q}_\mathrm{W}$, respectively
$\vec{P}_\mathrm{W}$, $\vec{Q}_\mathrm{W}$	induction arrows with Wiese's direction definition adopted, identical to, respectively, $\vec{P}$ and $\vec{Q}$ in eq. (3).
$\overrightarrow{PP}$	Parkinson arrow
$\overrightarrow{PW}$	Wiese arrow
T	period, $T=2\pi/\omega$
t	local time, UT
X, Y, Z	geographic North, geographic East, and vertical component of $\boldsymbol{B}$, respectively
Z_i	internally induced part of Z
z	depth
z_D, z_H	transfer functions relating Z_i to D_n and H_n, respectively
z_m	conductance integration depth
z^*	depth of perfect substitute conductor, subsect. 2.3.1.2, eq. (6)
α	azimuth of horizontal field component, measured clockwise from North
ϱ	electrical resistivity, in [Ωm]
ϱ_a	apparent electrical resistivity, subsect. 2.3.1.2, eqs. (1) and (2) for Schlumberger and induction methods, respectively
ϱ^*	(modified) apparent electrical resistivity, subsect. 2.3.1.2, eq. (7)
ϱ_T	transverse electrical resistivity, i.e. product of resistivity and thickness of resistive layer, in [Ωm^2]
σ	electrical conductivity, in [S/m]